# PHOTOCATALYTIC STUDY OF $WO_3$/rGO NANOCOMPOSITES ON CONGO RED DYE AND RHODAMINE B

Project report submitted to

MAHATMA GANDHI UNIVERSITY, KOTTAYAM

for the partial fulfilment of the requirements for the award of the degree of

MASTER OF PHILOSOPHY

IN

PHYSICS

RAJANI S NAIR

SMP20PHY006

DEPARTMENT OF PHYSICS

ST.TERESA'S COLLEGE (Autonomous), ERNAKULAM 682011

AUGUST 2022

Dr KALA M S
Professor
Department of Physics
St Teresa's College (Autonomous)
Ernakulam 682011

# CERTIFICATE

This is to certify that this dissertation entitled "PHOTOCATALYTIC STUDY OF $WO_3$/rGO NANOCOMPOSITES ON CONGO RED DYE AND RHODAMINE B" is a bonafide work carried out by RAJANI S NAIR (Reg. No. SMP20PHY006) under my supervision and guidance in partial fulfilment of the requirements for the Degree of Master of Philosophy in Physics at St Teresa's College (Autonomous), Ernakulam affiliated to Mahatma Gandhi University, Kottayam.

Dr KALA M S

(Supervising Guide)

# DECLARATION

I RAJANI S NAIR, hereby declare that this dissertation entitled "PHOTOCATALYTIC STUDY OF $WO_3$/rGO NANOCOMPOSITES ON CONGO RED DYE AND RHODAMINE B" is based on the original work done by me at the Department of Physics, St Teresa's College (Autonomous), Ernakulam. The work presented in this dissertation has not been submitted for the award of any other degree or diploma elsewhere.

RAJANI S NAIR

Date:

Place: Ernakulam

# ACKNOWLEDGEMENT

I express my profound gratitude to **Dr Kala M S,** Professor, St Teresa's College, Ernakulam for her valuable advice and suggestions. Her professional guidance, expertise and encouragement throughout the course of the work has helped me to complete the same. I express my sincere gratitude to all the teachers and non-teaching staff, St Teresa's College, Ernakulam for their help and co-operation throughout my work. I thank my batch mates Mrs Merly Ann Peter, Ms Anjaly Ravi, Ms Anakha M, Sr Achal Grace and Ms Farzana for their support and help.

I hereby express my sincere gratitude to the supervising guide of my Aspire project **Dr Reshmi R**, Assistant Professor, UC College, Aluva for providing me with necessary facilities to carry out the project work. The joy of getting acquainted with a group of well associated, highly efficient research fellows in Department of Physics, UC College, Aluva was a great experience. I express my sincere thanks to all the research students.

I would like to acknowledge the **Department of Collegiate Education** (DCE) for funding me through the Aspire Scholarship. I would like to acknowledge the **STIC India, Cochin University of Science and Technology and C-MET** for the characterizations done.

I take this opportunity to thank my family members for their love and blessings showered upon me.

# POWER POINT PRESENTATION

- Presented a power point entitled “Photocatalytic activity of metal oxide/2D layered structures with $WO_3$ nanocomposites” in the International E-Symposium on Sustainable Energy: Advances and Developments, E-Sensol 2022 organised by UANL on 8$^{th}$ July 2022.

- Presented a power point entitled “Synthesis of 2D layered structures with metal oxide nanocomposites for photocatalytic applications” in the Annual Physics Symposium, APS 2022 organised by the Department of Physics, St Teresa’s College (Autonomous), Ernakulam on 18$^{th}$ March 2022.

# ABSTRACT

Metal oxides are widely used in photocatalytic applications mainly for the decomposition of toxic compounds and environmental pollutants. The degradation is pollution free and therefore helps in environmental protection and produces harmless by products.

In the present study tungsten trioxide ($WO_3$) based photocatalyst were synthesized which possesses excellent chemical stability. Tungsten trioxide based photocatalyst were synthesized by doping $WO_3$ with Ag forming Ag-$WO_3$ and doping $WO_3$ with rGO forming rGO-$WO_3$ using hydrothermal method. The ternary compound Ag-$WO_3$-rGO was synthesized using a two-step hydrothermal method. The hydrothermal method was chosen as it was simple and efficient. The characterisation of the samples were done using XRD, SEM, EDX and Raman spectroscopy.

The photocatalytic activity of the above synthesized nanocomposites were evaluated by the degradation of Congo red dye and Rhodamine B dye. Pure $WO_3$ was added to the dye and the degradation of the dye when exposed to visible light was noted after 60 min. It was seen that the dye has shown very less degradation. In further study pure $WO_3$ was doped with silver and with rGO and the resulting sample was dissolved in Congo red dye. The % degradation with Silver doped $WO_3$ was higher compared with rGO doped $WO_3$ when exposed to visible light for 60 min. The experiment was repeated with ternary Ag-$WO_3$-rGO also. The results show that Ag-$WO_3$ and ternary nanocomposite show excellent degradation of Congo red dye under visible irradiation.

The photocatalytic study was repeated with Rhodamine B dye also. The % degradation of the dye was more effective with Ag-$WO_3$ and ternary nanocomposite. The degradation efficiency was observed more in the case of Congo red dye within a given time interval compared with Rhodamine B dye.

The enhanced photocatalytic activity usually can be due to three aspects: the increased adsorption of dye molecules, the enhanced light absorption and the increased band gap after doping. When $WO_3$ is doped with Ag, it is seen that Ag acts as an electron reservoir that effectively contributes for enhancing the photocatalytic performance of Ag-$WO_3$. In the case of rGO-$WO_3$ the addition of rGO into $WO_3$ would increase the specific surface area of photocatalyst which will enhance the photocatalytic activity.

# CONTENT

# FIGURES

# TABLES

# PREFACE

Chapter 1 deals with the classification of nanomaterials. It describes the harmful effects of water pollution and the importance of waste water treatment in the present situation. It describes the importance of photocatalyst in various fields for waste water treatment and antibacterial applications. The importance of metal oxide nanoparticles and two dimensional layered materials are well explained. This chapter also explains the various methods adopted to synthesize 2D materials.

Chapter 2 describes the experimental procedure for synthesizing the nanomaterials. The various characterisation techniques like XRD, SEM, EDX and Raman spectroscopy were explained. Each characterisation techniques have its own unique instrumentation and working. This chapter gives a detailed idea of the instrumentation and working of various characterisation techniques.

Chapter 3 includes the results and discussions .The results from XRD, SEM, EDX and Raman spectrum were analysed and discussed. The mechanism of photocatalytic activity and adsorption effects of the prepared samples in Congo red dye and Rhodamine B dye are well explained in this chapter.

# CHAPTER - 1

# INTRODUCTION

Nanotechnology is the study of material of size less than 100 nm or smaller at least in one dimension. The term “Nanotechnology” was first defined by a well-known scientist “Norio Taniguchi” of Science University, Tokyo, in a 1974 paper [1].

Nanomaterials are materials having one or more dimensions in the range of 100 nm or less. The classification of nanomaterials is based on the number of dimensions of the material that are outside the nanoscale range. They are broadly classified as

- Zero-dimensional
- One-dimensional
- Two-dimensional
- Three-dimensional

Zero-dimensional (0D) nanomaterials will have all the dimensions measured within the nanoscale and are generally termed as nanoparticles. One-dimensional (1D) nanomaterials will have one dimension outside the nanoscale. This includes nanotubes and nanowires. In two-dimensional (2D) nanomaterials, two dimensions are outside the nanoscale. This includes graphene, nanofilms and nano coatings. Three-dimensional (3D) nanomaterials are materials which are not confined to the nanoscale in any dimension. This includes bundles of nanowires and nanotubes.

Figure 1.1 shows some nanomaterials available in different morphological forms [1]

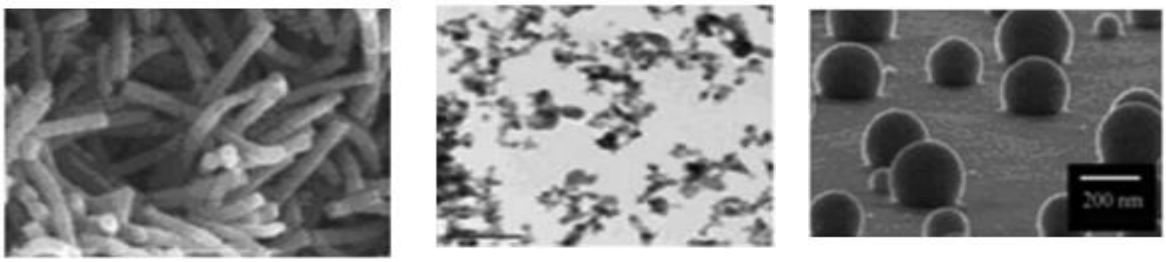


**Fig 1.1** Nanotube Polymeric nanoparticle Nanosphere

A nanocomposite is a multiphase material in which one of the phases has one or more dimensions less than 100nm. They have exceptionally high surface to volume ratio, exhibit quantum confinement effects and have enhanced electrical, magnetic and mechanical properties. It has increased ductility without decrease in mechanical strength and can be formed

by combining inorganic nanoclusters, clays, fullerenes, metals, oxides or semiconductors with various organic polymers and enzymes.

Carbon nanocomposites are composite material made of carbon and nanoparticles in nanoscale size. Figure 1.2 shows various types of carbon nanocomposites.

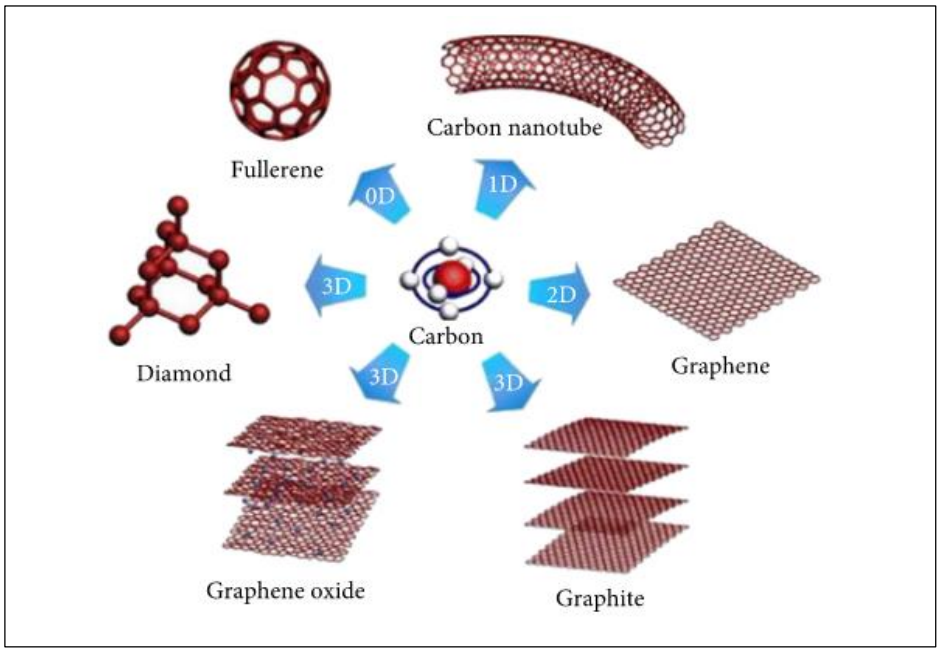


**Fig 1.2** Various types of carbon nanocomposites [2]

The physical and chemical properties of nanomaterials differ measurably than those of the bulk materials. The importance of nanomaterials lies in their vast increase in the surface area to volume ratio, which results in the possibilities of new quantum mechanical effects. One such example is the change in the electronic properties of solids due to the large reduction in particle size. Quantum confinement effects can also change the electrical conductivity, specific heat, and band gap of the nanomaterials. Physical properties of bulk material also change when it reaches the nanoscale. In some cases the changes are not desirable. For example, ferroelectric materials smaller than 10 nm can switch their magnetization direction using room temperature thermal energy, and thus making it useless for memory storage[1]. Nanoparticles made up of metals, semiconductors, or oxides shows excellent photocatalytic activities which are of great interest in the field of research.

Over the past few decades, billions of people are suffering from carcinogenic diseases, infections and allergies caused by impure water contaminated with harmful dyes and microorganisms. Lack of safe drinking water has put the human societies in trouble. Apart from

this it has created harm to the aquatic life also. This has compelled scientists working in this field to develop new materials with novel strategies to overcome this serious issue. The ultrafine nanomaterials have been used as photo catalysts in various fields for waste water treatment and antibacterial applications [3].

Photocatalysis has gained considerable attention over the years due to its applications in various fields. The most basic humanitarian goal is to provide pure water and to reduce and eliminate these non-biodegradable and toxic waste from water. Photocatalytic activity mainly depends on the ability of a catalyst to generate electron hole pairs. This process generates free radicals like hydroxyl radicals which undergoes secondary reactions.

The unusual properties and applications of metal oxide nanoparticles have attracted the attention of researchers in the present time. The increased surface area in nanostructured metal oxides lead to increased reactivity. Therefore more molecules of metal oxide nanoparticles are available on the surface for reacting with incoming molecules. Due to large surface area they are more sensitive to external stimuli like light.

$TiO_2$ is a widely used photocatalyst. $TiO_2$ based photocatalytic process is a low-cost, environmentally friendly process. In the case of $TiO_2$ the band gap is 3.2 eV, and it requires high ultraviolet radiation for excitation. This limits the application of $TiO_2$ in visible light region. Further the photocatalytic activities of $TiO_2$ is affected by the low quantum yield of excitons due to the fast electron-hole recombination and the recombination of radical intermediates on its surface. Several methods have been adopted for the improvement of photocatalytic activity of $TiO_2$. This involves doping $TiO_2$ with metals, non-metals, carbon-based nanoparticles and co-doping technique (simultaneous doping of two kinds of elements into $TiO_2$). Surface modification of $TiO_2$ with organic ligands also have proved to enhance the photocatalytic activity of $TiO_2$ [4].

Many articles suggest that tungsten trioxide ($WO_3$) and its nanocomposites have attracted popularity in recent years because of its outstanding properties. Tungsten trioxide ($WO_3$), a transition metal oxide is an oxygen deficient n type wide band gap semiconductor material with band gap of 2.6 – 3.5 eV [5] and can be activated by visible light irradiation. It is nontoxic, chemically and photo chemically stable and has diversely tunable stoichiometry and structures. It can form different compounds like $WO_3$, $WO_2$ etc. due to the existence of multiple oxidation

numbers. The molecular weight of $WO_3$ was generally observed to be 231.838 g/mol, density is 7.2 g/cm$^3$, and melting point is about 1473$^0$C. It is soluble in water and ammonia [6].

$WO_3$ nanoparticles have high specific area and good surface permeability which helps in using it for wide range of applications like gas sensors, photo catalyst and field emission devices [7]. The $WO_3$ crystal structures can be dependent on temperature. It is tetragonal in structure at temperature above 740$^0$C, orthorhombic from 330$^0$C to 740$^0$C, monoclinic from 17$^0$C to 330$^0$C and triclinic from -50$^0$C to 17$^0$C [8]. The most common structure of $WO_3$ is monoclinic.

$WO_3$ have some drawbacks due to relatively low energy density, smaller specific surface area and high recombination rate of photo generated electron hole pairs which limit its photo catalytic activity. These drawbacks can be improved by developing various $WO_3$ – based composite materials to improve their performance. It can be done by doping it with two dimensional layered materials like graphene and transition metals [9].

Two dimensional layered materials are of great interest in the field of research due to its large surface active applications. These materials consist of different layers and each of these layers are coupled through vander waals interactions. The electrons in these layers are free to move in the 2D plane. Any material can thin down till it has thickness of few atoms. Some materials which have bonds oriented in 3D requires cutting of these bonds. The 2D materials prepared by this method will have high density dangling bonds that are chemically unstable. Graphene (an allotrope of Carbon), phosphorene (P), silicene (Si), germanene (Ge), stanine (Sn) are some examples of 2D materials. Compound 2D materials include hexagonal boron nitride (h-BN), semiconducting Mo and W based transition metal dichalcogenides (TMDs), transition metal carbides and -nitrides (MXenes). Graphene and h-BN have 2D crystal structures with the same plane covalently bound in a hexagonal lattice whereas TMDs have three atoms and make an X-M-X sandwich in the form of trigonal prismatic [10].

Graphene is an allotrope of carbon which exists in two dimensional sheet form. The carbon atoms in graphene are bound to each other by hexagonal bonds along planes within the bulk material. These planes are stacked one above the other and can be separated without leaving dangling bonds. Due to the absence of dangling bonds, the charge carrier scattering is reduced in the 2D materials as compared with the bulk material. Due to strong interlayer coupling, the electronic band structure of the 2D materials is highly dependent on the thickness of the layer

[10]. It has various properties like high surface area, high mechanical strength and excellent electrical and thermal conductivities [11].

Graphene oxide (GO) is the oxidised form of graphene. The structure of GO sheets is a continuous and atomically thin, two-dimensional (2D) array of carbon atoms that is functionalised with epoxy and hydroxy groups on the carbon basal plane, and carboxy groups around the edges. The major part of the basal plane consists of carbon domains which are relatively hydrophobic. The acidic edges are considered to be hydrophilic and hence GO is considered to have amphiphilic structure [12]. The various defects brought to graphene structure create on-plane functionalization defects and in-plane lattice defects in the GO's σ-framework of the hexagonal lattice [13]. Due to these unique properties, GO has wide applications in photocatalysis, solar cells and hydrogen storage.

GO can be synthesized from the oxidation and exfoliation of graphite. The most accepted method is the modified Hummer's method. Reduced graphene oxide (rGO) is another form of GO in which the oxygen content is reduced by using chemical, thermal and other methods. The structure of graphene, GO and rGO is given in figure 1.3.

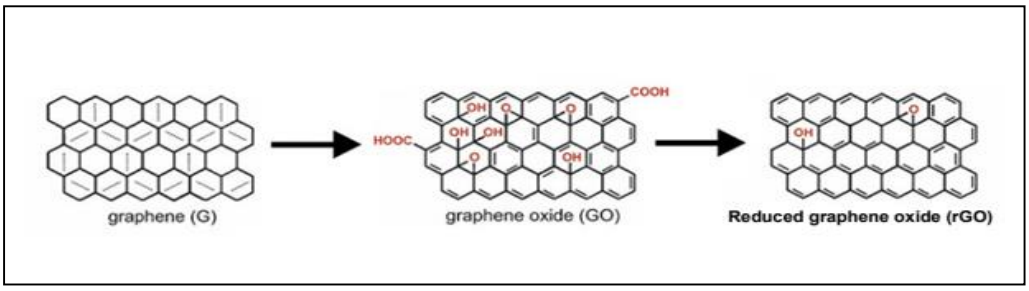


**Fig 1.3** Structures of Graphene, Graphene oxide and reduced graphene oxide [12]

Transition metals like silver also plays an important role in increasing the photocatalytic activity of $WO_3$ due to the enhanced charge separation and electron hole recombination reduction. When $WO_3$ is exposed to irradiation, electrons from the valence band moves to the conduction band thereby creating holes in the valence band. When the semiconductor $WO_3$ is doped with transition metal like silver, electrons from the semiconductor shifts to the metal if the fermi energy level of the semiconductor is higher than that of the metal particle. The accumulation of the electrons on the metal surface drives the reactions on the catalyst. The metal nanoparticles also have better affinity to many reactants than semiconductor. The light

absorption property of fine silver nanoparticles is due to the localized surface plasmon resonance (LSPR) effect of the transition metal nanoparticles. LSPR is the resonant photon-induced coherent oscillation of charges at the metal/dielectric interface, when the frequency of the photon becomes equal to the natural frequency of the oscillating metal surface electrons. For small particles, a resonantly enhanced uniform field builds up inside the particle producing a dipolar field outside the particle. This leads to enhanced absorption and scattering cross sections for electromagnetic waves [14].

Various methods are adopted to synthesize ultrathin 2D materials and it can be generally divided into two categories,

- Bottom-up methods
- Top-down methods

Bottom-up approach deals with the build-up of a material from the bottom: atom-by-atom, molecule-by-molecule. It is more economical as it produces less waste. Bottom up methods include hydrothermal, solvothermal methods, sol-gel synthesis and colloidal precipitation.

Top-down approach involves the breaking down of the bulk material into nanosized particles. It depends on miniaturization of bulk fabrication processes to produce the desired structure with suitable properties. Liquid exfoliation assisted by mechanical force, heat, oxidation and selective etching, electron beam lithography and atomic force manipulation are some examples of top down methods.

In this work, a bottom up approach – specifically the hydrothermal method has been employed for the synthesis of $WO_3$ and composites. The method involves the synthesis of substance by chemical reactions in a sealed and heated aqueous solution or organic solvent filled in a specially sealed container or high-pressure autoclave at appropriate temperature and pressure (1-100 MPa) [15].

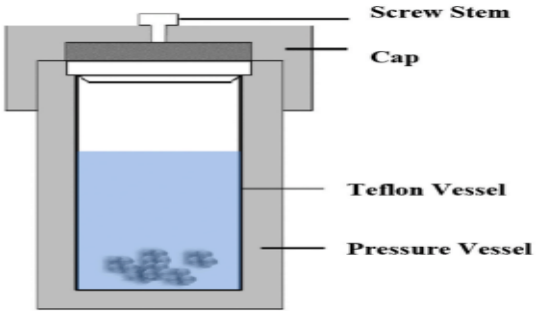


**Fig 1.4** Schematic diagram of autoclave [16]

Rhodamine B (RhB) and Congo red are two dyes widely used in textile industry and effluents from the factories are reported to contaminate water to a great extent. RhB is a water-soluble fluorescent xanthene dye with a chemical structure of $C_{28}H_{31}ClN_2O_3$. The molecular weight of RhB is observed as 479.02 g/mol and the wavelength ($\lambda_{max}$) at which maximum absorption occurs for the dye is obtained at 543nm [17]. It is widely used in industrial purposes, such as printing and dyeing in textile, paper, paints etc.

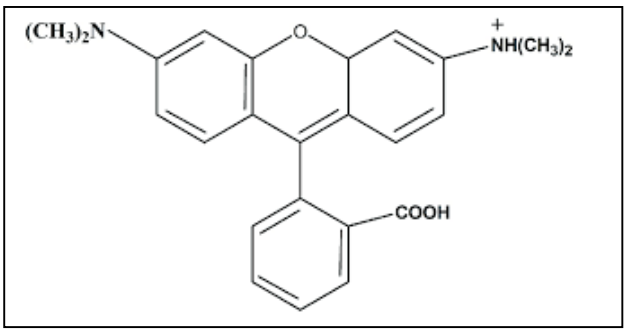


**Fig 1.5** Chemical structure of Rhodamine B [17]

Congo red dye is a water-soluble azo dye with a chemical structure of $C_{32}H_{22}N_6Na_2O_6S_2$. The molecular weight of Congo red dye is observed as 696.665 g/mol and the wavelength ($\lambda_{max}$) of maximum absorption is obtained at 497nm [18].

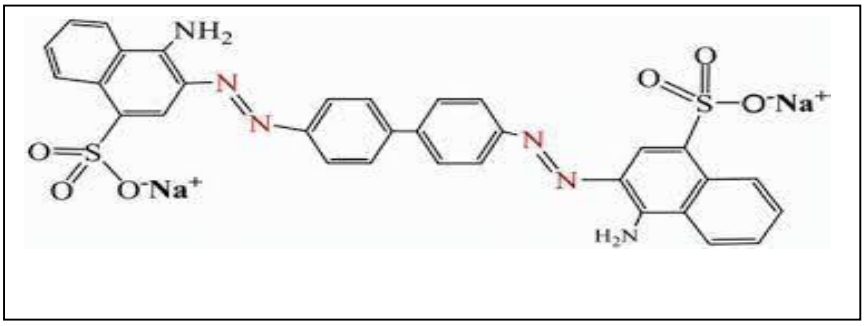


**Fig 1.6** Chemical structure of Congo red dye [18

Congo red dye shows a colour change from blue to red corresponding to pH value 3 to 5.2. and can therefore be used as a pH indicator also. It is used in cotton industry as a dye as well as for staining tissues for microscopic examination in the field of histology.

# REFERENCES


(1) Visakh, P. M., and María José Martínez Morlanes. *Nanomaterials and nanocomposites: zero-to three-dimensional materials and their composites*. John Wiley & Sons, 2016.

(2) Veeman, Dhinakaran, M. Varsha Shree, P. Sureshkumar, T. Jagadeesha, L. Natrayan, M. Ravichandran, and Prabhu Paramasivam. "Sustainable development of carbon nanocomposites: synthesis and classification for environmental remediation." *Journal of Nanomaterials* Vol.2021, Article ID 5840645, 21 pages, 2021.

(3) Bhat, Shahnawaz Ahmad, Fahmina Zafar, Aftab Hossain Mondal, Abdul Kareem, Azar Ullah Mirza, Shabnam Khan, Abdulrahman Mohammad, Qazi Mohd Haq, and Nahid Nishat."Photocatalytic degradation of carcinogenic Congo red dye in aqueous solution, antioxidant activity and bactericidal effect of NiO nanoparticles." *Journal of the Iranian Chemical Society* 17, no. 1 (2020): 215-227.

(4) Dong, Haoran, Guangming Zeng, Lin Tang, Changzheng Fan, Chang Zhang, Xiaoxiao He, and Yan He. "An overview on limitations of $TiO_2$-based particles for photocatalytic degradation of organic pollutants and the corresponding countermeasures." *Water research* 79 (2015): 128-146.

(5) Najafi-Ashtiani, Hamed, Ali Bahari, Samira Gholipour, and Siamak Hoseinzadeh. "Structural, optical and electrical properties of $WO_3$–Ag nanocomposites for the electro-optical devices" *Applied Physics Article* 124, no. 1 (2018): 1-9.

(6) Wang, Shea-Jue, Mu-Chun Wang, Shih-Fan Chen, Yu-Hsiang Li, Tien-Szu Shen, Hui-Yun Bor, and Chao-Nan Wei. "Electrical and physical characteristics of $WO_3$/Ag/$WO_3$ sandwich structure fabricated with magnetic-control sputtering metrology." *Sensors* 18, no. 9 (2018): 2803.

(7) Besnardiere, Julie, Binghua Ma, Almudena Torres-Pardo, Gilles Wallez, Houria Kabbour, José M. González-Calbet, Hans Jürgen Von Bardeleben, Benoit Fleury, Valerie Buissette, Clement Sanchez, Thierry Le Mercier, Sophie Cassaignon and David Portehault. "Structure and electrochromism of two-dimensional octahedral molecular sieve h'-$WO_3$." *Nature communications* 10, no. 1 (2019): 1-9.

(8) Rao, M. C. "Structure and properties of $WO_3$ thin films for electrochromic device application." *J. Non-Oxide Glasses* 5 (2013): 1-8.

(9) Nguyen, Cong Tu, Tuan Phong Pham, Thi Lan Anh Luu, Xuan Sang Nguyen, Thanh Tung Nguyen, Huu Lam Nguyen, and Duc Chien Nguyen. "Constraint effect caused by

graphene on in situ grown Gr@ $WO_3$-nanobrick hybrid material" *Ceramics International* 46, no. 7 (2020): 8711-8718.

(10) Kumar, Chandan, Santanu Das, and Satyabrata Jit. "Device physics and device integration of two-dimensional heterostructures." In *2D Nanoscale Heterostructured Materials*, pp. 195-214. Elsevier, 2020.

(11) Yoshida, Naoko, Yasushi Miyata, Yuko Goto, Yuji Nagao, Ryugo Tero, and Akira Hiraishi. "Graphene oxide-dependent growth and self-aggregation into a hydrogel complex of exoelectrogenic bacteria." *Scientific reports* 6, no. 1 (2016): 1-11.

(12) McCoy, Thomas M., Geosmin Turpin, Boon Mian Teo, and Rico F. Tabor. "Graphene oxide: a surfactant or particle?." *Current Opinion in Colloid & Interface Science* 39 (2019): 98-109.

(13) Sun, Ling. "Structure and synthesis of graphene oxide." *Chinese Journal of Chemical Engineering* 27, no. 10 (2019): 2251-2260.

(14) Sarina, Sarina, Eric R. Waclawik, and Huaiyong Zhu. "Photocatalysis on supported gold and silver nanoparticles under ultraviolet and visible light irradiation." *Green Chemistry* 15, no. 7 (2013): 1814-1833.

(15) Feng, S-H., and G-H. Li. "Hydrothermal and solvothermal syntheses." In *Modern inorganic synthetic chemistry*, pp. 73-104. Elsevier, 2017.

(16) Ijaola, Ahmed Olanrewaju, Peter Kayode Farayibi, and Eylem Asmatulu. "Superhydrophobic coatings for steel pipeline protection in oil and gas industries: A comprehensive review." *Journal of Natural Gas Science and Engineering* 83 (2020): 103544.

(17) Oyekanmi, Adeleke Abdulrahman, Akil Ahmad, Kaizar Hossain, and Mohd Rafatullah. "Adsorption of Rhodamine B dye from aqueous solution onto acid treated banana peel: Response surface methodology, kinetics and isotherm studies." *PLoS One* 14, no. 5 (2019): e0216878.

(18) Das, Arijit, Sourav Bhattacharya, Gangotri Panchanan, B. S. Navya, and Parvathi Nambiar. "Production, characterization and Congo red dye decolourizing efficiency of a laccase from Pleurotus ostreatus MTCC 142 cultivated on co-substrates of paddy straw and corn husk." *Journal of Genetic Engineering and Biotechnology* 14, no. 2 (2016): 281-288.

# CHAPTER – 2

# METHODOLOGY

This chapter describes the synthesis methods employed to prepare the samples and also the techniques used for characterisation of these samples. In this work, the following samples have been prepared

- Graphene oxide (GO)
- Tungsten trioxide ($WO_3$)
- Ag doped $WO_3$ (Ag-$WO_3$)
- rGO doped $WO_3$ (rGO-$WO_3$)
- Ternary compound (Ag-$WO_3$-rGO)

## 2.1 MATERIALS

Sodium nitrate ($NaNO_3$), Sodium tungstate dihydrate ($Na_2WO_42H_2O$), and Silver nitrate ($AgNO_3$) were obtained from Merck, India. All the solutions were prepared using deionised (DD) water in the laboratory.

## 2.2 SYNTHESIS

Graphene oxide (GO) was synthesized using modified Hummer's method [1]. Tungsten trioxide ($WO_3$) and its nanocomposites, Ag-$WO_3$ and rGO-$WO_3$ were synthesized using hydrothermal method. Ternary nanocomposite, Ag-$WO_3$-rGO was synthesized using two step hydrothermal method.

### 2.2.1 GRAPHENE OXIDE

Graphene oxide was synthesized using modified Hummer's method. 2g of graphite flakes and 2g of $NaNO_3$ were mixed in 90ml of $H_2SO_4$ (98%) in 1000ml volumetric flask kept under ice bath with continuous stirring. The mixture was stirred for 4hrs at this temperature and 12g of $KMnO_4$ was added to the suspension very slowly. The temperature was controlled below 15$^oC$. The mixture was diluted with slow addition of 180ml water and kept under stirring for 2hrs. The ice bath was then removed and the mixture was then stirred at 35$^oC$ for 2hrs.

The above mixture was kept on a magnetic stirrer and stirred at 98$^0C$ for 10 minutes, after which the temperature was changed to 30$^0C$ and the resulting solution changes to a brown

colour. Again after 10min the temperature was changed to $25^0$C and maintained it for 2hrs. The solution was finally mixed with 40ml of $H_2O_2$ and the colour of the solution turned bright yellow.

The prepared solution was then taken in two beakers and mixed with 200ml of DD water, kept without stirring for 3-4hrs and allowed the particles to settle at the bottom. The solution was washed with DD water for two to three weeks till its pH is 6 [1].

### 2.2.2 TUNGSTEN TRIOXIDE

For the preparation of tungsten trioxide, 0.4g (400mg) of $Na_2WO_42H_2O$ was dissolved in 10ml of DD water. Then 5ml 35% HCl was then slowly added in 10ml of this mixture with continuous stirring. The mixture was then transferred to 50ml Teflon steel autoclave and kept at $140^0$C for 8h. After 8h, the sample was allowed to cool to room temperature, washed with DD water and ethanol several times. Then the sample was dried in an oven at $70^0$C overnight.

### 2.2.3 Ag - $WO_3$

For the preparation of Ag - $WO_3$, 25ml $Na_2WO_4$ solution was prepared by dissolving 0.4g of $Na_2WO_42H_2O$ in 25ml DD water at room temperature under continuous stirring after which 5ml nitric acid was poured to form a yellow suspension. Then 0.84g of Silver nitrate was dissolved in 50ml of DD water and stirred for 4h and transferred into a 100ml Teflon lined steel autoclave. The hydrothermal process was carried out at $180^0$C for 24h. After cooling, the solution was filtered several times with DD water and dried at $80^0$C for 12h.

### 2.3.4 rGO - $WO_3$

For the preparation of rGO - $WO_3$, the already prepared GO was dispersed in DD water with the help of ultrasonicator forming a suspension of concentration 0.5mg per ml. 5ml of 35% HCl was added slowly and then transferred to a Teflon lined steel autoclave. The hydrothermal process was carried out at $140^0$C for 8h. After cooling, filtered several times with DD water and dried at $80^0$C for 12h.

### 2.2.5 TERNARY COMPOUND Ag-$WO_3$-rGO

For the preparation of ternary Ag-$WO_3$-rGO, 200mg of GO was dissolved in 50ml of DD water and ultrasonicated for 10min.Then 100mg of already prepared Ag doped $WO_3$ was added to the GO solution and sonicated for 5min to make a homogeneous suspension. The mixture was

transferred into a 100ml Teflon lined steel autoclave and the hydrothermal process was carried out at $180^0$C for 24h. After cooling, filtered several times with DD water and dried at $80^0$C for 12h.

## 2.3 CHARACTERISATION TECHNIQUES

Characterisation is an important method for identifying the structure and chemical composition of materials. They include X-ray diffraction, scanning electron microscopy (SEM), transmission electron microscopy (TEM), X-ray fluorescence spectroscopy (XRF), NMR and other synchrotron techniques. X ray diffraction technique is one of the efficient methods for determining the structure of materials. Various other techniques such as Fourier transform Infra-red spectroscopy (FTIR), Raman spectroscopy etc. are used for structural analysis. The characterisation methods employed in this study are discussed in detail below.

### 2.3.1 X-Ray diffraction

X-ray diffraction is one of the prominent techniques for determining the atomic and molecular structure of crystalline materials. This technique involves a scattering process in which X-rays are scattered by the electrons of the atoms present in the material without changing the wavelength. The resulting diffraction pattern, given by the positions and intensities of the diffraction effects gives an idea of the structure of the material. The diffraction of electrons by the crystal lattice is governed by Bragg's law given by,

$$2d \sin\theta = n\lambda \quad \text{..... (2.1)}$$

where, d is the interplanar spacing of the lattice planes with Miller indices (hkl)

θ is the glancing angle

n is the order of diffraction

λ is the wavelength of X-rays

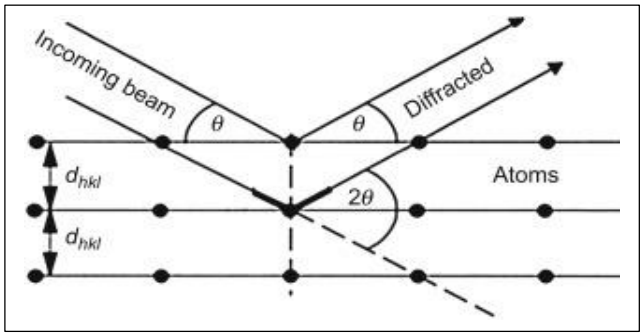


**Fig 2.1** Geometrical condition for diffraction from lattice planes [2]

The sample is scanned through an angle 2θ and a graph is plotted with diffraction angle 2θ along the X axis and diffraction intensity along the Y axis. The diffraction pattern will have various peaks corresponding to several planes of same order which satisfies Bragg's law equation. The 'd' value can be found for each peak and then comparing the 'd' value and the angle 2θ with the standard reference JCPDS files, the material can be identified.

### 2.3.2 Instrumentation and Working

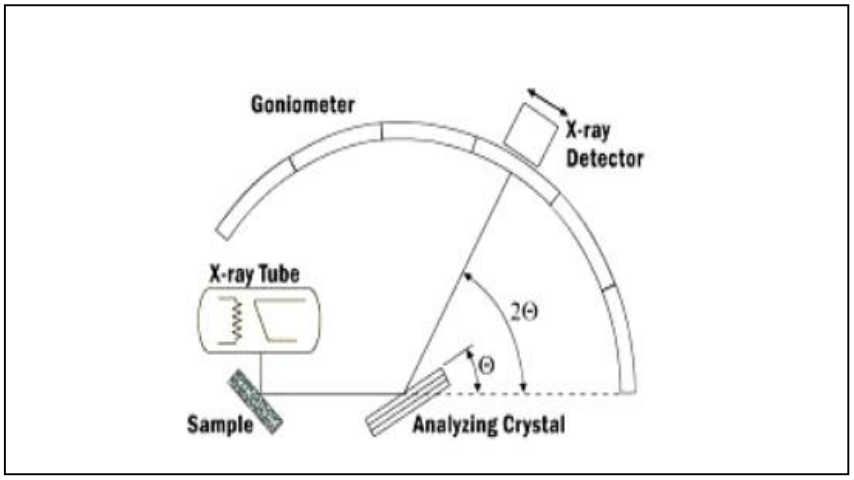


**Fig 2.2** Schematic diagram of a diffractometer [3]

Most of the XRD devices work based on the reflection geometry which involves X-ray source and detector on the same side of the sample. The scattered X-rays from the X-ray tube are reflected from the sample and then incident on the detector. The scattered X-rays undergo constructive interference.

The filament in the cathode ray tube is heated to produce the high energy electrons. These electrons are then collided with the target materials. The high energetic electrons now penetrate into the target material and remove the innermost electrons which creates vacancy in the

innermost shell. These vacancies are filled by the electrons in the outermost shell. This transition results in the release of X-ray photon. The wavelength of the X-rays depends on the target material. The transition of the electrons from the outermost shells results in different lines like $K_\alpha$ and $K_\beta$ in the characteristic spectra of X-rays. The produced X-rays can be collimated and directed towards the sample. The sample can be rotated in the direction of collimated X-rays at an angle θ while the detector can be rotated at an angle 2θ. This device is called goniometer. The detector now processes the X-ray signals and sends the data to the computer. In general, the diffraction data are represented as intensity distribution as a function of the 2θ angle as represented by the figure 2.3.

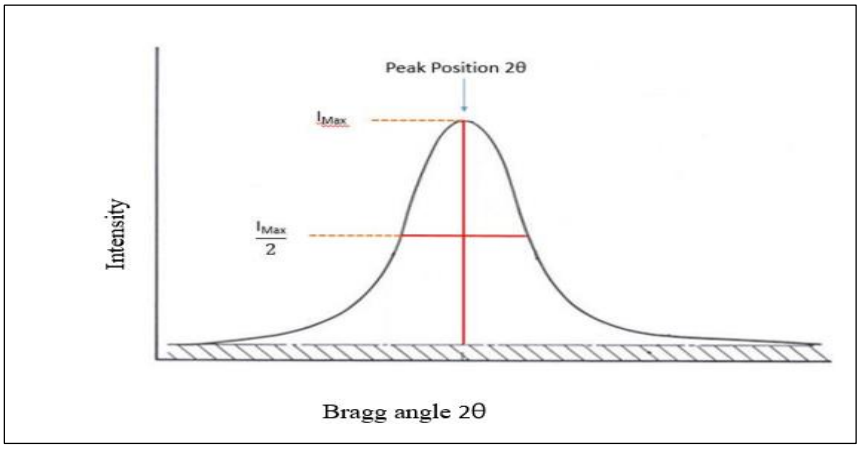


**Fig 2.3** Half width peak intensity [4]

The crystalline structure of the material can be determined by the XRD. The broadening of peaks shows the deviation from crystallinity. The crystalline size is determined by the Scherrer formula given by,

$$B_c = \frac{K\lambda}{L\cos\theta} \quad \text{..... (2.2)}$$

where K is the Scherrer constant

λ is the wavelength of X-rays

L is the crystalline size

$B_c$ is the peak width (full width at half maximum)

### 2.3.3 Raman spectroscopy

Raman spectroscopy is a type of vibrational spectroscopy employed for the identification of elements in the sample. A monochromatic light source, usually from a laser in the visible, near infrared or near ultraviolet region can be used. When light interacts with the molecules of matter, majority of the photons are scattered at the same energy as that of the incident photon. This type of scattering is described as elastic scattering or Rayleigh scattering. Few number of photons scatter at a frequency other than the incident photon frequency and this process is called inelastic scattering or Raman scattering. When the change in the energy of the scattered photon is less than the energy of the incident photon, the scattering is called Stokes scattering while the change in energy is greater than the energy of the scattered photon, it is called anti-Stokes. On the opposite sides of the Rayleigh line, the Stokes and anti-Stokes lines exists as mirror images. The difference in the frequency between the Raman lines and Rayleigh lines is used to measure the vibrational energy of the system.

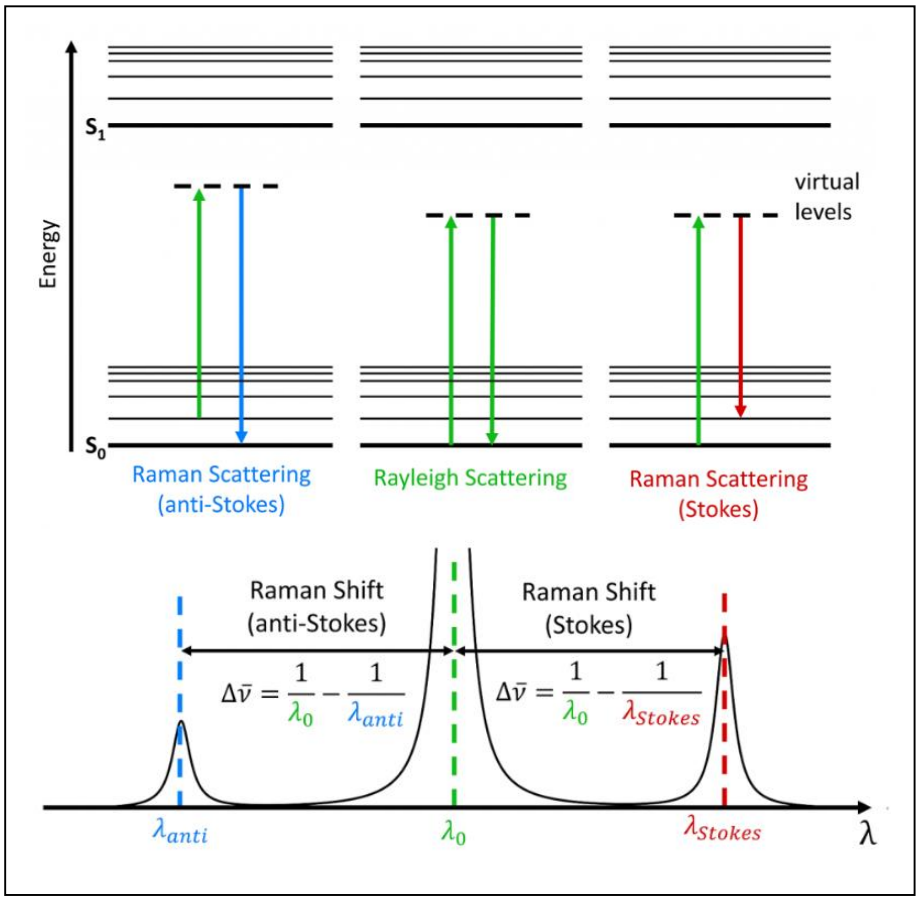


**Fig 2.4** Diagram showing the origin of Rayleigh, anti-Stokes and Stokes lines [5]

Raman spectroscopy is used for analysing low frequency modes in a system. It gives the information about the vibrational modes of system under consideration. It is more used as a structural characterisation technique than a chemical analysis technique. The detection of structural defects, alloy fluorescence etc. can be done with Raman spectroscopy. It can be used for detecting the stress in semiconductor materials and devices.

### 2.3.4 Scanning Electron Microscope (SEM)

Scanning electron microscope is a type of electron microscope that uses a focused beam of electrons to produce images of the sample. The basic components of SEM are

(i) An electron gun consisting of cathode and anode

(ii) The condenser lens that controls the amount of electrons

(iii) The objective lens focusing the beam of electrons on the sample

(iv) Secondary electron detector that attracts the secondary electrons

(v) Deflection coil to deflect the electrons

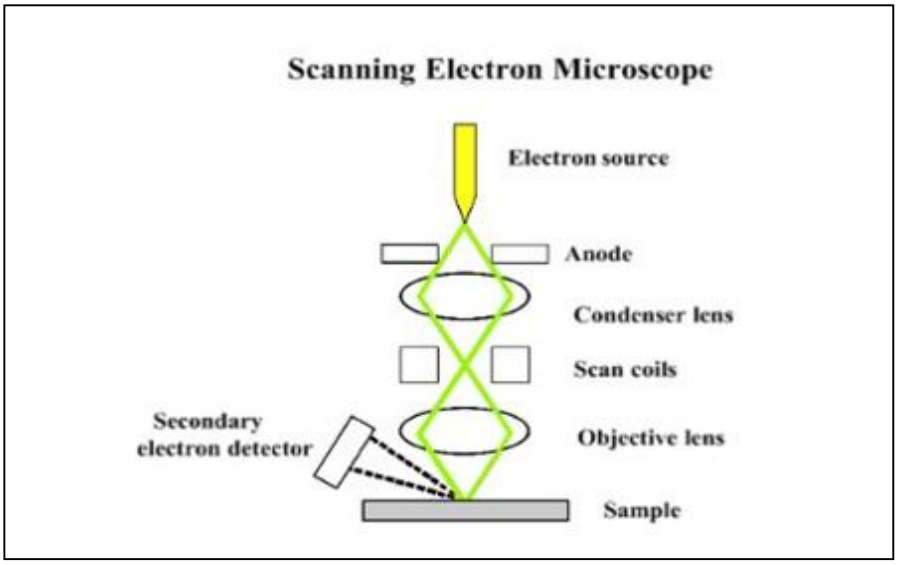


**Fig 2.5** Schematic representation of SEM [6]

### (i) Electron Gun

The electron beam is produced by the electron gun which consists of a filament made of tungsten wire which acts as the cathode. By heating the filament at a very high temperature, thermo electrons are produced. A metal plate which acts as an anode is maintained at a positive voltage up to 30 kV gathers the electron beam. A wehnelt electrode maintained at negative

voltage, kept between the cathode and anode adjusts the current of the electron beam and focuses it. Schottky – emission and field-emission guns can also be used as electron guns [7].

(ii) **Condenser lens**

Condenser lens is kept below the electron gun and controls the diameter of the electron beam. A metal plate with a hole in the middle is kept between the condenser lens and objective lens. The electron beam when passes through the condenser lens illuminates the aperture plate. The adjustment of the excitation of the condenser lens helps to change the electron probe diameter. If the excitation of the condenser lens is decreased, the electron beam becomes narrower and most of the electrons pass through the aperture [7].

**(iii) Objective lens**

Objective lens is used to find the electron probe diameter. It focuses the electron beam to the sample.

**(iv) Secondary electron detector (SED)**

The secondary electrons emitted from the sample are detected by secondary electron detector. The detector has a scintillator coating to detect the electrons. When the electron reaches the scintillator, it produces light flashes and the light guide directs the light to a photo multiplier tube which converts the light to electrons and amplifies it to electrical signals.

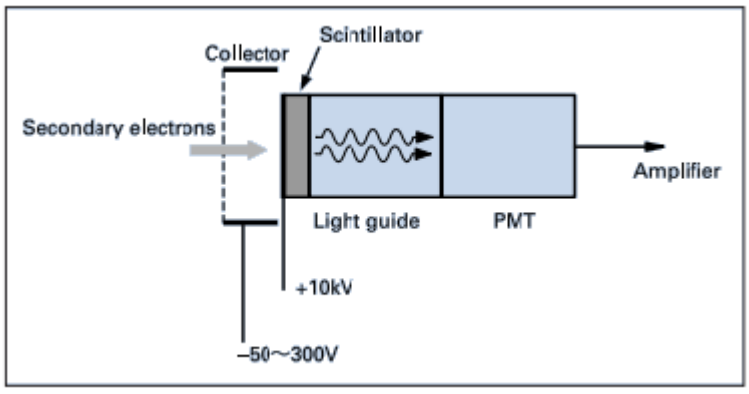


**Fig 2.6** Secondary electron detector [7]

**(v) Deflection coil**

The deflection coils are used to deflect or tilt the electron beam.

**Working**

A beam of electrons is produced on the top of the microscope using the electron gun which travels through the electromagnetic fields and lenses and is focused on the sample. When the beam of electrons hits the sample, electrons and X-rays are ejected from the sample. The back scattered electrons, secondary electrons and the X-rays are collected by the detector and converted them into a signal that is sent to a screen.

### 2.3.5 UV-Visible absorption spectrophotometry

UV-Visible spectroscopy is an analytical technique in which the amount of light absorbed at each wavelength of UV and visible regions of the electromagnetic spectra is measured. Absorption spectroscopy deals with the wavelength ranging from 190nm to 800nm. The absorption of light by molecules results in molecular excitations thereby exciting the electrons from lower energy level to higher energy level. The relationship between the energy of light absorbed and the frequency of light is given by,

$$E = h\nu \quad \text{.....(2.3)}$$

where E is the energy of photon

h is the Planck's constant

υ is the frequency of photon

**Beer-Lambert Law**

When a monochromatic light of incident intensity $I_0$ is transmitted through a solution, the transmittance, T of the solution is given by,

$$T = \frac{I}{I_0} \quad \text{..... (2.4)}$$

where I is the transmitted intensity

The absorbance, A, of the solution is related to the incident and transmitted intensities by,

$$A = log_{10} \frac{I_0}{I} = -log_{10} T \quad \text{.....(2.5)}$$

where $I_0$ is the incident intensity

I is the transmitted intensity

The absorbance has a logarithmic relation to the transmittance. The transmittance is 100% corresponding to an absorbance of 0 and 10% transmittance corresponding to an absorbance of 1. More combinations of absorbance of solution and transmittance are possible.

The Beer-Lambert law gives a linear relationship between the concentration and absorbance of solution. So by measuring the absorbance, the concentration of the solution can be calculated. The absorbance of the solution is given by,

$$A = \varepsilon c l \quad \text{..... (2.6)}$$

where ε is the molar absorption coefficient

c is the molar concentration

l is the optical path length

**Construction and working**

The basic components of UV-Visible absorption spectrophotometer are

(i) Light source
(ii) Wavelength selector
(iii) Sample analyser
(iv) Detector
(v) Computer

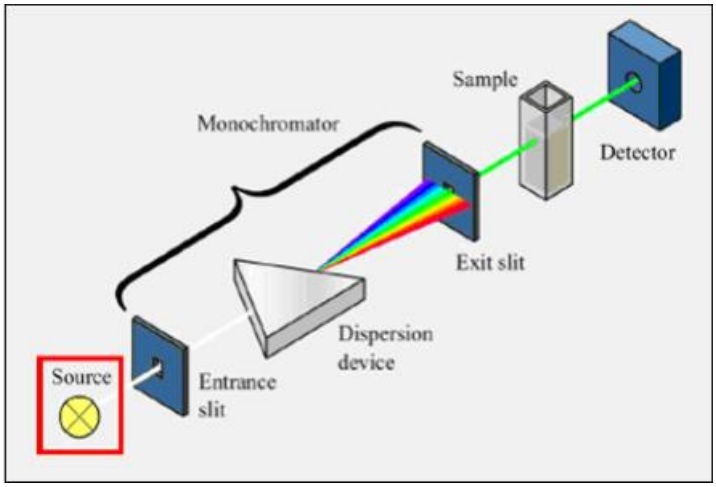


**Fig 2.7** Schematic diagram of UV-Visible absorption spectrophotometer [8]

Light from the source is focused to the slit of the monochromator which uses optical grating to separate the light by wavelength. Then the light is passed through a detector where the intensity of light at each wavelength can be measured.

## 2.4 Photocatalytic Studies

The photocatalytic activity of the prepared samples has been investigated by photodegradation study of Rhodamine B and Congo red dye under visible light illumination. The light source used was halogen light bulb (50W, 220V). The solution was prepared by mixing 1mg of the dye in 100 ml of DD water (10 ppm). Each photocatalyst sample (25mg) was added to 10mL of dye taken in a beaker, which was maintained at $25^0$C by using ice cubes and cold water. Before exposing to light, the dye solution was stirred for 10 min in the darkness to reach an adsorption-desorption equilibrium. The mixture was then exposed to light. After each interval of 20 min, the mixture was centrifuged to remove the photocatalysts. The supernatant was used to monitor the photo-degradation efficiency (PDE) of the dye. The degradation efficiency of the dye was determined by the equation (2.7)

$$PDE(\%) = \frac{C_0 - C_t}{C_0} \times 100 = \frac{I_0 - I_t}{I_0} \times 100 \quad \text{..... (2.7)}$$

where $C_0$ is the initial concentration of dye (mg/L) and $C_t$ is the concentration of dye (mg/L) at a definite interval of time at the end of each experiment; $I_0$ is the intensity of the maximum peak in UV-Vis spectrum of initial dye solution; $I_t$ is the intensity of the maximum peak in UV-Vis spectrum at a definite interval of time at the end of each experiment. The intensity of maximum peak corresponds to 501 nm in the case of prepared Congo red dye and 557 nm in the case of prepared Rhodamine B dye.

# REFERENCES

(1) Paulchamy, Balaiah, G. Arthi, and B. D. Lignesh. "A simple approach to stepwise synthesis of graphene oxide nanomaterial." *J Nanomed Nanotechnol* 6, no. 1 (2015): 1.

(2) Rao, M. C. "Structure and properties of $WO_3$ thin films for electrochromic device application." *J. Non-Oxide Glasses* 5 (2013): 1-8.

(3) Bunaciu, Andrei A., Elena Gabriela UdriŞTioiu, and Hassan Y. Aboul-Enein. "X-ray diffraction: instrumentation and applications." *Critical reviews in analytical chemistry* 45, no. 4 (2015): 289-299.

(4) Fatimah, Siti, Risti Ragadhita, Dwi Fitria Al Husaeni, and Asep Bayu Dani Nandiyanto. "How to calculate crystallite size from x-ray diffraction (XRD) using Scherrer method." *ASEAN Journal of Science and Engineering* 2, no. 1 (2010): 65-76.

(5) Mohammed Harshulkhan, S., K. Janaki, G. Velraj, R. Sakthi Ganapthy, and M. Nagarajan. "Effect of Ag doping on structural, optical and photocatalytic activity of tungsten oxide ($WO_3$) nanoparticles." *Journal of Materials Science: Materials in Electronics* 27, no. 5 (2016): 4744-4751.

(6) Thermo Fisher Scientific, Antonis Nanakondis, What is SEM? Scanning Electron Microscopy Explained, (14-Nov-2019).

(7) Jeol, serving advanced technology, "Scanning electron microscope A to Z." Basic knowledge for using the SEM, http://www.jeol.com/

(8) Gohain, Neelakshi. "Studies on the structure and function of phenazine modifying enzymes PhzM and PhzS involved in the biosynthesis of pyocyanin." PhD diss., 2009.

# CHAPTER – 3

# RESULTS AND DISCUSSIONS

## 3.1 XRD ANALYSIS

XRD of the prepared samples were taken using the X-ray diffractometer Bruker AXS D8 Advance. Fig 3.1(a) shows the XRD pattern of GO and fig 3.1(b) shows the XRD pattern of Graphite given for comparison from ref [1].

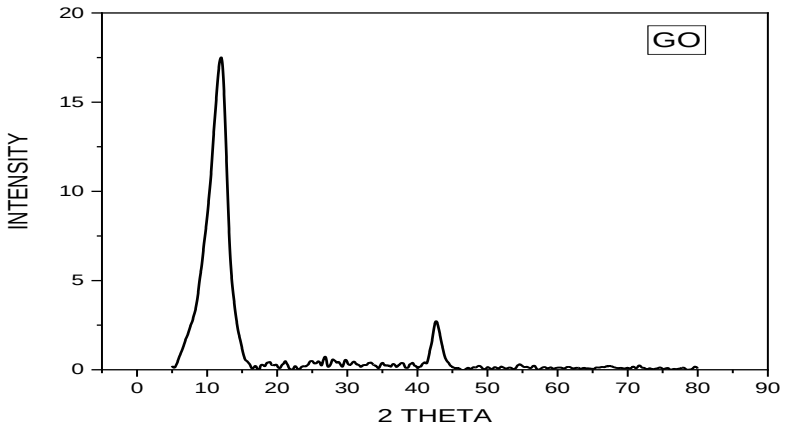


**Fig 3.1(a)** XRD of GO

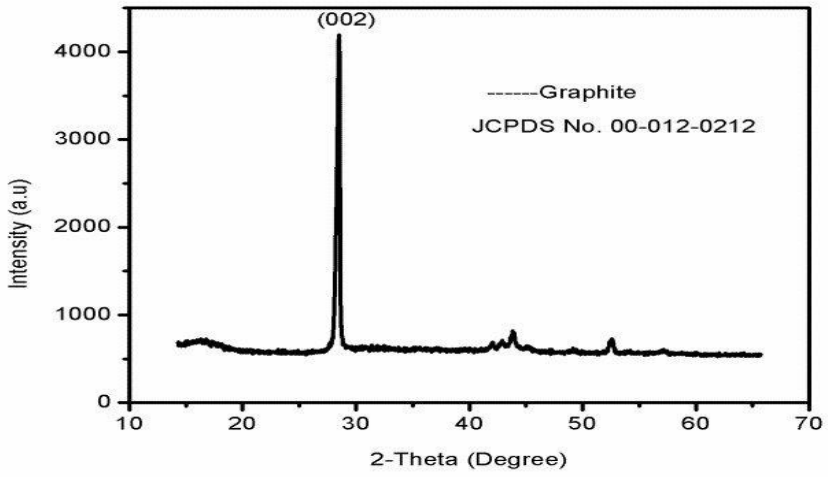


**Fig 3.1(b)** XRD of Graphite [1]

The XRD spectrum of GO shows a high intense peak at $2\theta = 11.59^0$, indicating the formation of Graphene oxide structure. Comparing with the XRD spectrum of Graphite given in fig 3.1(b), it can be observed that graphite shows peak at $2\theta = 26.6^0$[1] and the shifting of peak in the case of Graphene oxide towards the left is due to the oxidation of graphite. Fig 3.2 shows the XRD patterns of $WO_3$, Ag-$WO_3$, rGO-$WO_3$ and the ternary sample Ag-$WO_3$-rGO.

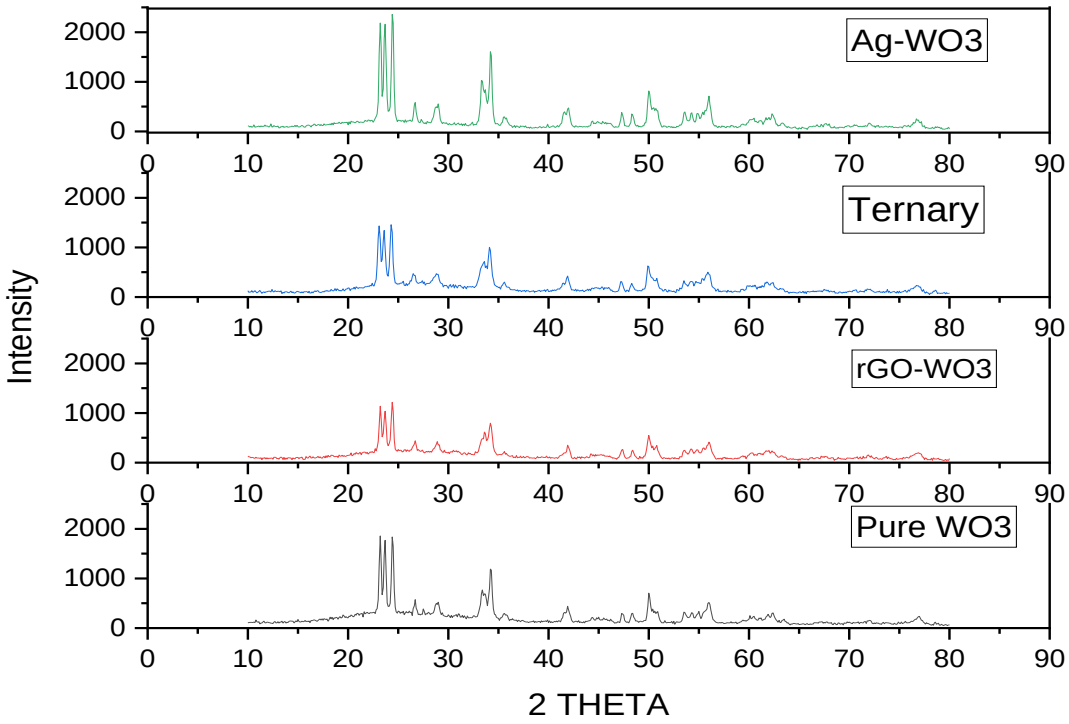


**Fig 3.2** XRD patterns of $WO_3$, Ag-$WO_3$, rGO-$WO_3$ and the ternary sample Ag-$WO_3$-rGO

In the XRD spectra of the ternary nanocomposite and rGO-$WO_3$, the diffraction peaks were not observed in the range from $10^0$ to $15^0$ showing that GO was completely reduced to rGO. The XRD patterns of the samples $WO_3$, Ag-$WO_3$, rGO-$WO_3$ and ternary Ag-$WO_3$-rGO were identical to each other substantiating that the direct incorporation of Ag and rGO does not affect the crystal structure of $WO_3$. The XRD peaks of $WO_3$, Ag-$WO_3$, rGO-$WO_3$ and ternary Ag-$WO_3$- rGO is listed in table 3.1. This is in agreement with the monoclinic structure of $WO_3$ as per the standard JCPDS file no.43-1035. Pure $WO_3$, Ag-$WO_3$, rGO-$WO_3$ and ternary nano composites can be indexed to the standard pattern of monoclinic $WO_3$ with the lattice constants a = 7.300 $A^0$, b = 7.538 $A^0$, c = 7.689 $A^0$ and $\beta = 90.892\ A^0$. Ag nanoparticles have XRD peaks at around $38^0$, $46^0$, $64^0$ etc. The monoclinic $WO_3$ also possesses peaks around these values and they are not observed due to the overlap.

**Table 3. 1.** XRD peaks of $WO_3$, Ag-$WO_3$, rGO-$WO_3$ and ternary Ag-$WO_3$- rGO

| Samples | $WO_3$ | Ag-$WO_3$ | rGO-$WO_3$ | Ternary |
|---|---|---|---|---|
| hkl planes | 2θ | | | |
| (020) | $23.70^0$ | $23.75^0$ | $23.58^0$ | $23.58^0$ |
| (200) | $24.39^0$ | $24.39^0$ | $24.39^0$ | $24.39^0$ |
| (120) | $26.65^0$ | $26.75^0$ | $26.65^0$ | $26.65^0$ |
| (112) | $28.93^0$ | $28.97^0$ | $28.82^0$ | $28.82^0$ |
| (022) | $33.46^0$ | $33.46^0$ | $33.65^0$ | $33.65^0$ |
| (202) | $34.00^0$ | $34.21^0$ | $34.21^0$ | $34.21^0$ |
| (220) | $35.56^0$ | $34.51^0$ | $34.48^0$ | $34.48^0$ |
| (222) | $41.83^0$ | $41.83^0$ | $41.83^0$ | $41.83^0$ |
| (004) | $47.44^0$ | $47.44^0$ | $47.44^0$ | $47.44^0$ |
| (040) | $48.48^0$ | $48.48^0$ | $48.48^0$ | $48.48^0$ |
| (400) | $50.23^0$ | $50.04^0$ | $50.04^0$ | $50.04^0$ |
| (420) | $55.99^0$ | $55.99^0$ | $55.99^0$ | $55.99^0$ |

The particle size was calculated using Scherrer formula. The particle size of GO and $WO_3$ and its nanocomposites is given in table 3.2.

**Table 3. 2.** The particle size of GO, $WO_3$, Ag-$WO_3$, rGO-$WO_3$ and ternary Ag-$WO_3$- rGO

| SAMPLE | PARTICLE SIZE (nm) |
|---|---|
| GO | 2.3 |
| $WO_3$ | 6.52 |
| Ag-$WO_3$ | 5.56 |
| rGO-$WO_3$ | 5.64 |
| Ag-$WO_3$-rGO | 4.66 |

The XRD analysis shows that the crystalline size has reduced in the case of $WO_3$ nano composites. The decrease in the crystalline size will enhance the photo catalytic activity due to the increase in surface area thereby increasing the adsorption/desorption.

## 3.2 SEM

The morphology of the synthesized nanocomposites ws observed by SEM. Fig 3.3(a) to 3.3(e) shows the SEM images of $WO_3$, Ag-$WO_3$, rGO-$WO_3$, ternary nanocomposite and GO respectively. The SEM image of $WO_3$ and Ag-$WO_3$ shows that it has spherical morphology. It was observed that $WO_3$ nano particles were randomly distributed on rGO sheets in the case of rGO-$WO_3$.The SEM image of GO shows that the graphene sheets are exfoliated in graphene oxide.

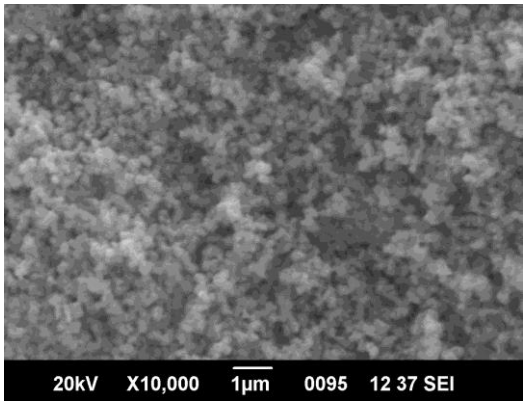


Fig 3.3 (a) SEM image of $WO_3$

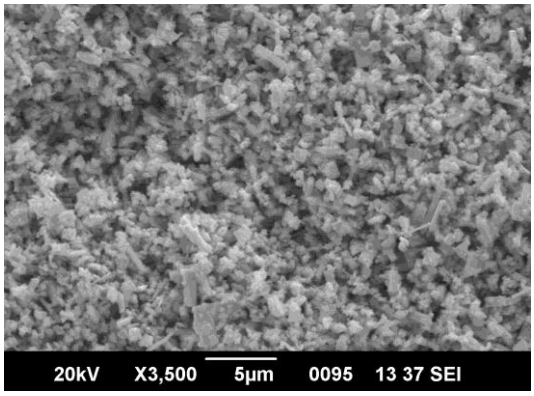


Fig 3.3 (b) SEM image of Ag-$WO_3$

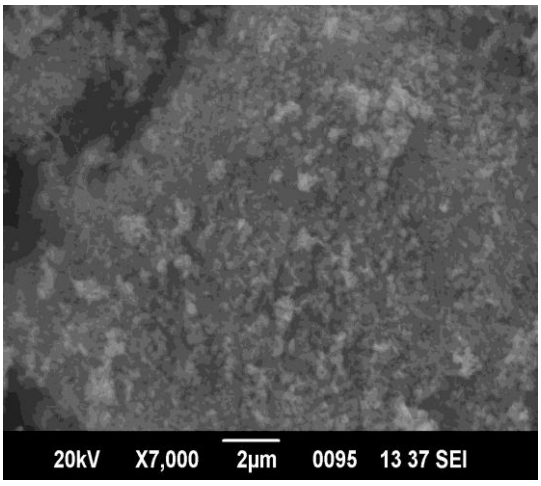


Fig 3.3 (c) SEM image of rGO-$WO_3$

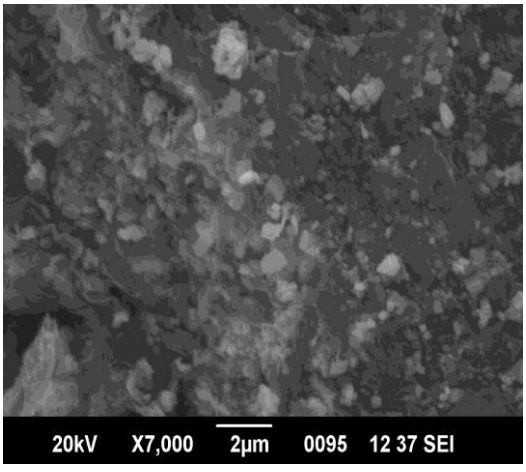


Fig 3.3 (d) SEM image of Ag-$WO_3$-rGO

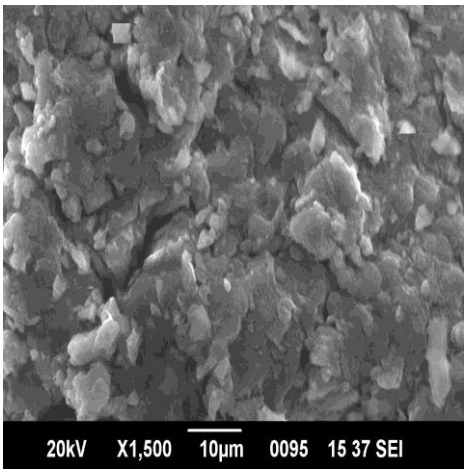


Fig 3.3 (e) SEM image of GO

The crystalline size calculated by Scherrer formula using XRD will be always less than the grain size using SEM. Crystalline size is the size of a single crystal in powder form whereas grain size is the size of a grain which can be either a single crystalline or polycrystalline material present in bulk form.

## 3.3 EDX

The elemental information of the prepared nanocomposite was analysed by EDX. Fig 3.4(a) shows the EDX of $WO_3$ which confirms the presence of elements tungsten and oxygen. Fig 3.4(b) shows the EDX of Ag-$WO_3$ which confirms the presence of silver in the synthesized material. It was observed that the intensity peak of tungsten was decreased due to the addition of silver ions in the tungsten site and intensity peak of oxygen remains constant for both pure and Ag doped $WO_3$ [2]. As shown in Fig 3.4(c), the EDX spectrum of rGO-$WO_3$ shows the existence of carbon, oxygen and tungsten indicating the formation of rGO-$WO_3$ nano composite [3]. Fig 3.4(d) shows the presence of carbon, oxygen, tungsten and silver.

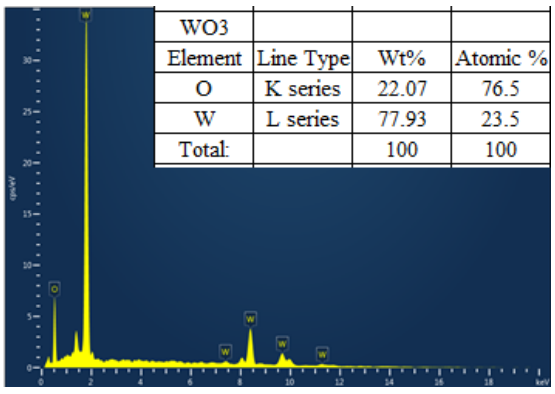

| WO3 | | | |
|---|---|---|---|
| Element | Line Type | Wt% | Atomic % |
| O | K series | 22.07 | 76.5 |
| W | L series | 77.93 | 23.5 |
| Total: | | 100 | 100 |

Fig 3.4(a) EDX spectrum of $WO_3$

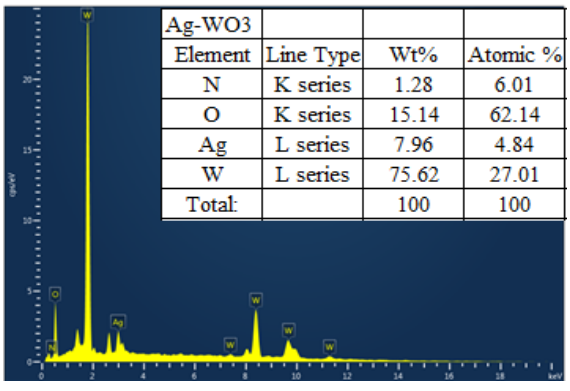

| Ag-WO3 | | | |
|---|---|---|---|
| Element | Line Type | Wt% | Atomic % |
| N | K series | 1.28 | 6.01 |
| O | K series | 15.14 | 62.14 |
| Ag | L series | 7.96 | 4.84 |
| W | L series | 75.62 | 27.01 |
| Total: | | 100 | 100 |

Fig 3.4(b) EDX spectrum of Ag-$WO_3$

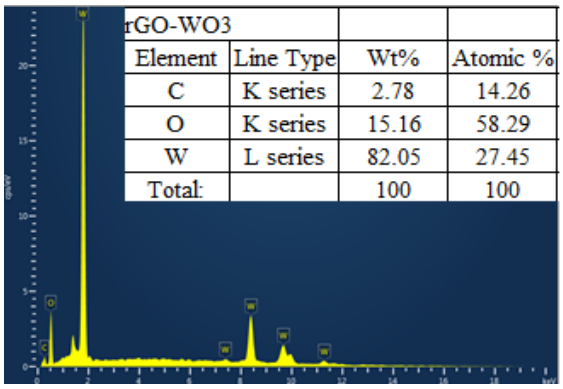

| rGO-WO3 | | | |
|---|---|---|---|
| Element | Line Type | Wt% | Atomic % |
| C | K series | 2.78 | 14.26 |
| O | K series | 15.16 | 58.29 |
| W | L series | 82.05 | 27.45 |
| Total: | | 100 | 100 |

Fig 3.4(c) EDX spectrum of rGO-$WO_3$

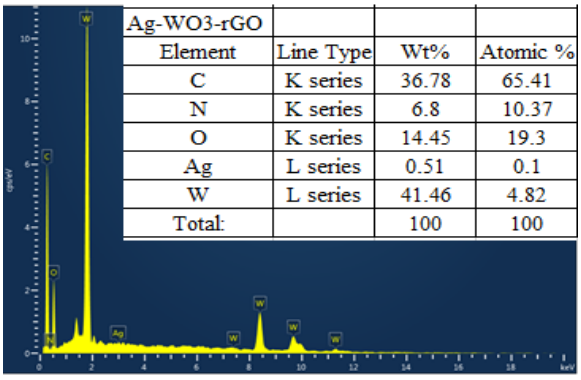

| Ag-WO3-rGO | | | |
|---|---|---|---|
| Element | Line Type | Wt% | Atomic % |
| C | K series | 36.78 | 65.41 |
| N | K series | 6.8 | 10.37 |
| O | K series | 14.45 | 19.3 |
| Ag | L series | 0.51 | 0.1 |
| W | L series | 41.46 | 4.82 |
| Total: | | 100 | 100 |

Fig 3.4(d) EDX spectrum of Ag-$WO_3$-rGO

## 3.4 RAMAN SPECTRUM

Fig 3.5 shows the Raman spectrum of GO and fig 3.6 shows the Raman spectrum of $WO_3$, Ag-$WO_3$, rGO-$WO_3$ and ternary Ag-$WO_3$-rGO.

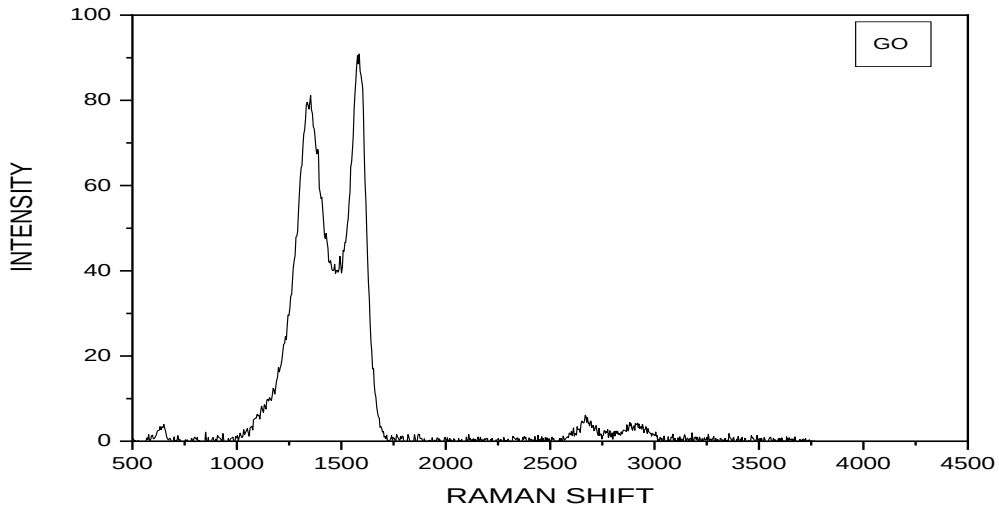


**Fig 3.5** Raman spectrum of GO

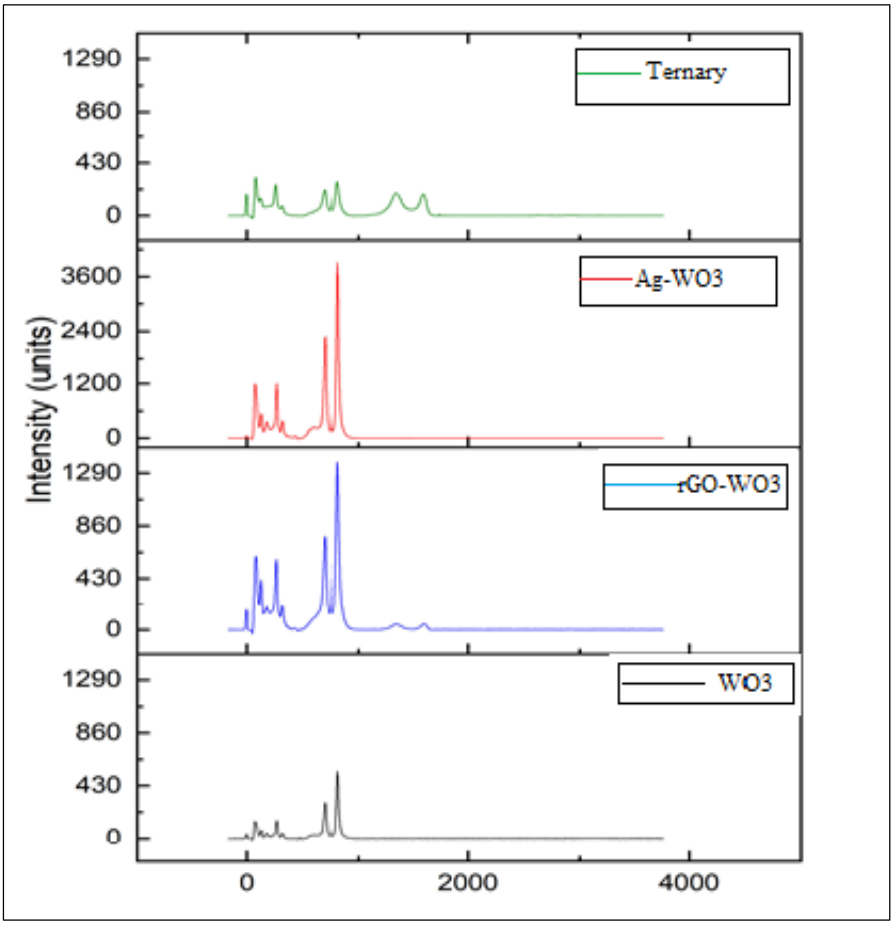


**Fig 3.6** Raman spectrum of $WO_3$ and its nano composites

The position of the characteristic Raman peaks of $WO_3$, Ag-$WO_3$, rGO-$WO_3$, Ternary Ag-$WO_3$- rGO and GO are listed below in the table 3.3:

**Table 3.3** Characteristic Raman peaks of $WO_3$, Ag-$WO_3$, rGO-$WO_3$, Ternary and GO

| Bonds | $WO_3$ | Ag-$WO_3$ | rGO-$WO_3$ | Ternary | GO |
|---|---|---|---|---|---|
| δ(O-W-O) | 272 | 270 | 272 | 247 | - |
| δ(O-W-O) | 328 | 324 | 328 | 322 | - |
| υ(W-O) | 716 | 716 | 708 | 710 | - |
| υ(O-W-O) | 804 | 804 | 804 | 799 | - |
| D band | - | - | 1344 | 1341 | 1341 |
| G band | - | - | 1598 | 1595 | 1579 |

According to table 3.3, the Raman peaks at 272,716 and 804 $cm^{-1}$ confirms the monoclinic structure of $WO_3$. Some peaks of $WO_3$ were seen shifted to the lower wavenumber when $WO_3$

was doped with Ag. This blue shift is due to the shortening of W-O bonds caused by the appearance of Ag.

While analysing the Raman spectra of GO, the presence of D band and G band was observed at 1341cm$^{-1}$ and 1579 cm$^{-1}$ respectively.

The Raman spectrum of rGO-$WO_3$, exhibits two bands at 1344 cm$^{-1}$ and 1598 cm$^{-1}$ corresponding to the graphite(G) and diamondoid(D) bands respectively. The same bands were observed in the case of rGO also. These bands are characteristic features of rGO nano composites. The G band corresponds to the tangential vibrations of the carbon atom and the D band is the standard sign of the presence of defective graphite carbon [2]. The same bands were observed in the case of ternary nanocomposite also.

It was observed that when rGO was introduced to Ag-$WO_3$, there is a red shift of the G band from 1579 cm$^{-1}$ to 1595 cm$^{-1}$ in the case of ternary Ag-$WO_3$-rGO nano composite. The corresponding shift in the case of rGO -$WO_3$ is 1598 cm$^{-1}$. This may be due to the hole transfer between rGO and $WO_3$/Ag which supplies the strong interaction between the components in the nanocomposite [4,5].

## 3.5 Optical properties

The absorption spectra of $WO_3$, Ag-$WO_3$, rGO-$WO_3$ and Ag-$WO_3$-rGO samples are given in Fig.3.7.

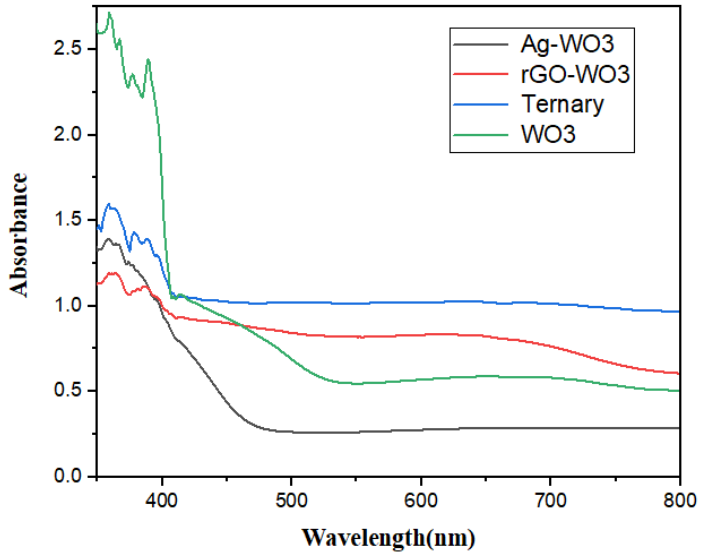


**Fig 3.7** Absorption spectra of $WO_3$ and its nanocomposites

It can be observed that the spectra of all the samples exhibit a characteristic absorption band around 400 nm, indicating the existence of highly crystallized $WO_3$.

Tauc's diagram was used to calculate the optical band gap of the samples. The equation is given by

$$(\alpha h\nu) = B(h\nu - E_g)^n \quad \text{..... (3.1)}$$

where α is the absorption coefficient calculated from absorbance using the equation $\left(\alpha = \frac{4\pi k}{\lambda}\right)$

where λ is the wavelength of incident photon

hν is the energy of the incident photon

n = ½ or 2 for direct and indirect recombination respectively

B is an arbitrary coefficient

$E_g$ is the optical band gap of the sample

Since $WO_3$ is an indirect band gap semiconductor, the band gap energy have been calculated by plotting $(\alpha h\nu)^{1/2}$ as a function of the photon energy hν. In the case of rGO-$WO_3$, the plot was drawn with $(\alpha h\nu)^2$ as a function of the photon energy hν. The extrapolated band gap of $WO_3$, Ag-$WO_3$ and rGO-$WO_3$ are 2.2 eV, 1.4 eV and 1.3 eV respectively.

Fig 3.8(a) and 3.8(b) shows the Tauc plot from which the band gap of $WO_3$, Ag-$WO_3$ and rGO-$WO_3$ were measured.

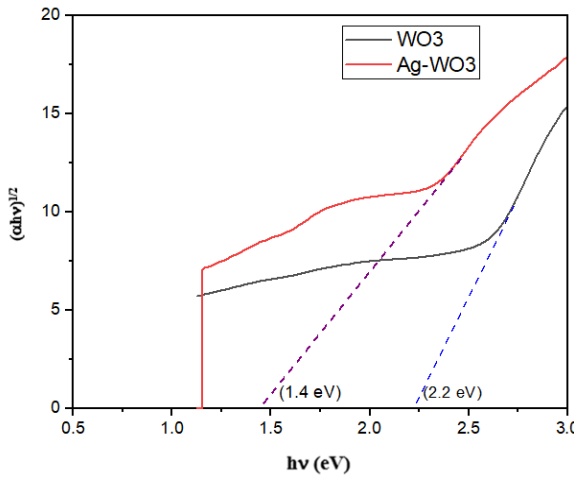


**Fig 3.8(a)** Tauc plot of $WO_3$ and Ag-$WO_3$

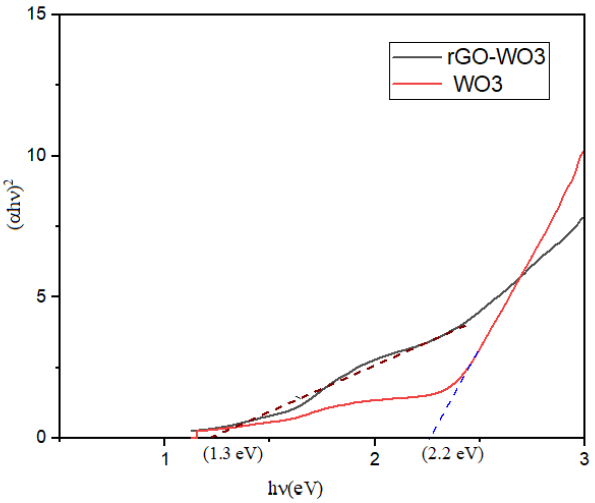


**Fig 3.8(b)** Tauc plot of $WO_3$ and rGO-$WO_3$

## 3.6 Photocatalytic study and Adsorption effects of $WO_3$ and its nanocomposites

### 3.6.1 Photocatalytic study on Congo red dye

The photocatalytic activity of the samples has been evaluated by measuring the absorbance changes caused by the degradation of Congo red dye for 60 min under visible light irradiation. For photodegradation of Congo red dye, 25 mg of the prepared samples, $WO_3$, Ag-$WO_3$ and rGO-$WO_3$ were added into 10 mL of the prepared Congo red dye solution and kept under dark conditions for 10 min. After light illumination at regular intervals, the suspension was taken and the photocatalyst was separated by centrifugation. The absorption of Congo red dye was then measured by a UV-Vis spectroscopy. Fig. 3.9(a) to Fig. 3.9(c) shows the photocatalytic activity of $WO_3$, Ag-$WO_3$ and rGO-$WO_3$ respectively. The degradation efficiency of the dye was determined by the equation (3.2)

$$PDE(\%) = \frac{C_0 - C_t}{C_0} \times 100 = \frac{I_0 - I_t}{I_0} \times 100 \quad \text{..... (3.2)}$$

The degradation rate of Congo red dye with $WO_3$ photocatalyst has shown 35.73% within 60 min of illumination, whereas $WO_3$ doped with Ag, exhibits a much higher degradation efficiency of 63.33%. Ag-$WO_3$ has shown 71.96% degradation efficiency within 90 min of illumination. The incorporation of $WO_3$ nanoparticles with rGO sheets also have increased the degradation efficiency by 56.86% within 60 min illumination.

For further study of photodegradation of Congo red dye, 10 mg of the prepared ternary nanocomposite, Ag-$WO_3$-rGO was added into 10 mL of the Congo red dye solution and the process was repeated. The synergistic combination of adsorption and photocatalytic activity by Ag-$WO_3$-rGO results in almost complete degradation of Congo red dye within 120 min under visible irradiation. This result indicates that Ag-$WO_3$, rGO-$WO_3$ and ternary Ag-$WO_3$-rGO nanocomposite shows improved photocatalytic activity for the effective treatment of organic dye pollutants compared with pure $WO_3$. The enhanced photocatalytic activity usually can be due to three aspects: the increased adsorption of dye molecules, the enhanced light absorption and the efficient charge separation. The photocatalytic activity of the ternary Ag-$WO_3$-rGO nanocomposite is shown in figure 3.9(d).

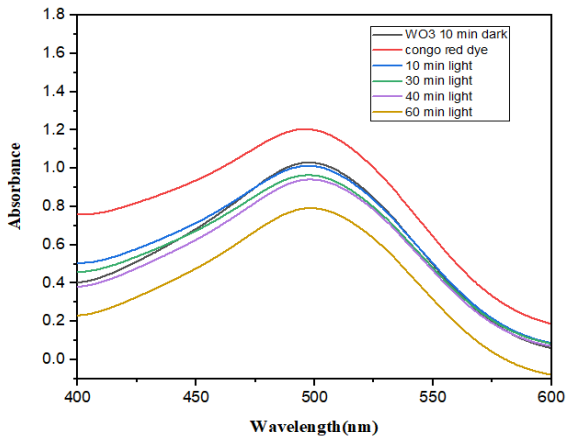


**(a)**

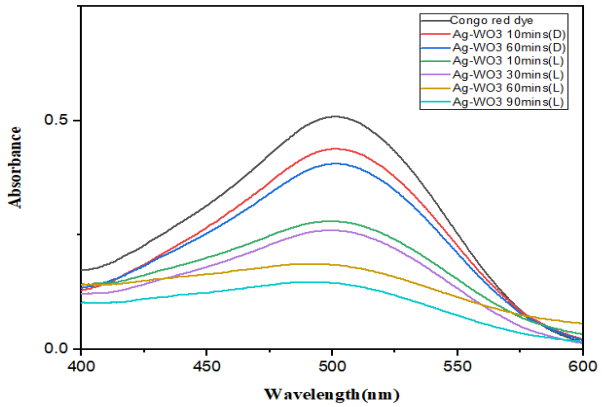


**(b)**

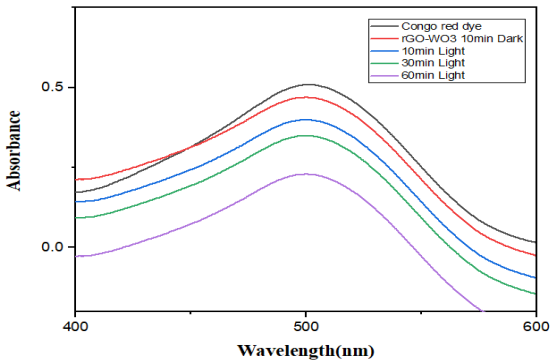


**(c)**

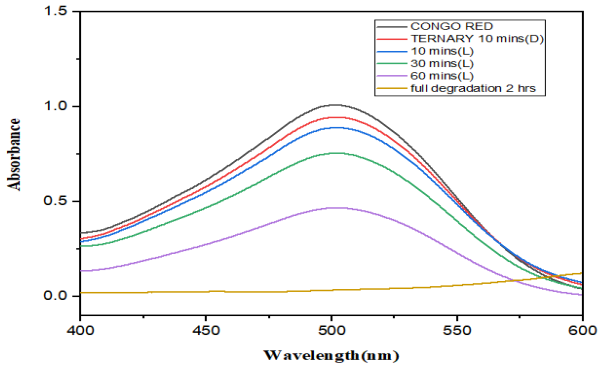


**(d)**

**Fig 3.9** Absorption spectra of Congo red dye in the presence of light (a) $WO_3$ (b) Ag-$WO_3$ (c) rGO-$WO_3$ (d) Ag-$WO_3$-rGO

Table 3.4 shows the degradation efficiency of the samples in Congo red dye. The degradation efficiency was observed as 63.33%, 56.86% and 35.73% for Ag-$WO_3$, rGO-$WO_3$ and $WO_3$ respectively within 60 min of visible light irradiation.

**Table 3.4.**Degradation efficiency of $WO_3$, Ag-$WO_3$, rGO-$WO_3$ and Ag-$WO_3$-rGO in Congo red dye

| **Samples** | **Time** | **Degradation efficiency** |
|---|---|---|
| TERNARY **(10 mg)** | 60 min | 53.4% |
| | 120 min | 96.73% |
| Ag-$WO_3$ **(25 mg)** | 60 min | 63.33% |
| | 90 min | 74.96% |
| rGO-$WO_3$ **(25 mg)** | 60 min | 56.86% |
| WO3 **(25 mg)** | 60 min | 35.73% |

Figure 3.10 shows the photocatalytic degradation of Congo red dye by $WO_3$, Ag-$WO_3$, rGO-$WO_3$ and ternary Ag-$WO_3$-rGO under visible irradiation within 120 min. It was observed that the % degradation efficiency was 35%, 65%, 77% and 95% in the case of $WO_3$, Ag-$WO_3$, rGO-$WO_3$ and ternary Ag-$WO_3$-rGO respectively.

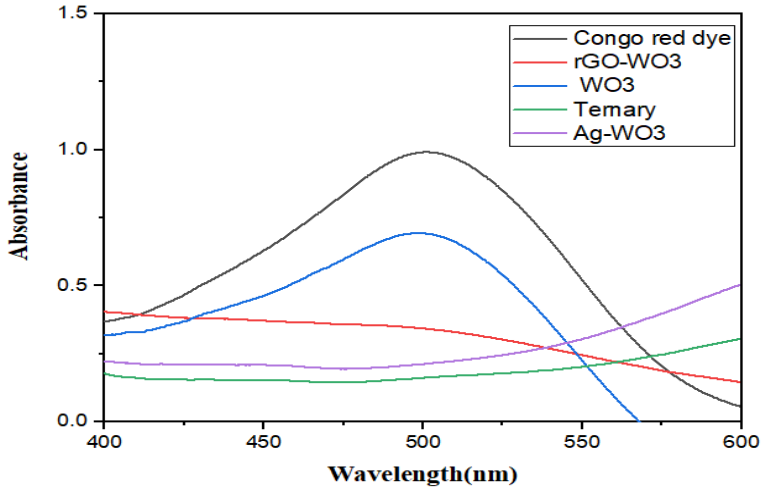


**Fig 3.10** Photocatalytic degradation of Congo red dye by $WO_3$ and its nanocomposites within 120 min

The degradation curve of Congo red with $WO_3$, Ag-$WO_3$, rGO-$WO_3$ and ternary Ag-$WO_3$-rGO under visible irradiation within 60 min is shown in Figure 3.11. In the figure time was plotted along the X axis, $\frac{C_t}{C_0}$ was plotted along the Y axis. $C_0$ (mg/L) is the initial concentration before irradiation by light and $C_t$ (mg/L) is the instantaneous concentration in the sample at time t. $C_0$ was measured as the intensity of the maximum peak in UV-Vis spectrum of initial dye solution, $C_t$ was measured as the intensity of the maximum peak in UV-Vis spectrum at a definite interval of time at the end of each experiment. The plot of $\frac{C_t}{C_0}$ and time is a straight line.

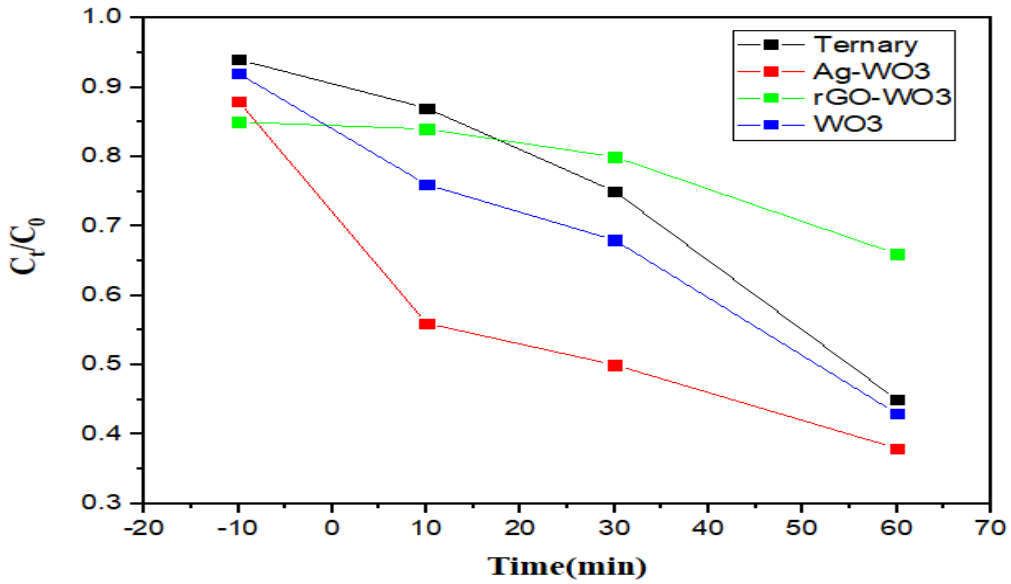


**Fig 3.11** Degradation curve of Congo red with $WO_3$ and its nanocomposite

### 3.6.2 Mechanism of photocatalytic activity of $WO_3$ and its nanocomposites on Congo red dye

Under visible light irradiation, most of the •OH radicals are generated directly from the reaction between the holes and surface adsorbed $H_2O$. The mechanism of photodegradation of Congo red dye is given by equations (3.3) and (3.4)

$$WO_3 + h\nu = h^+ + e^- \quad \text{(3.3)}$$

$$H_2O + h^+ = \bullet OH + H^+ \quad \text{(3.4)}$$

$$\text{Dye} + \bullet \text{OH} = \text{oxidation products}$$

Hole can also act as oxidant at higher concentrations

$$Dye + h^+ = \text{oxidation products}$$

### 3.6.3 Photocatalytic study on Rhodamine B

The degradation of Rhodamine B (RhB) dye was investigated by the prepared samples for 60 min under visible light irradiation. Ternary, Ag-$WO_3$ and rGO-$WO_3$ have shown improved photocatalytic activity compared with pure $WO_3$. Fig. 3.12(a) to Fig. 3.12(d) shows the photocatalytic activity of $WO_3$, Ag-$WO_3$, rGO-$WO_3$ and ternary nanocomposites respectively on RhB.

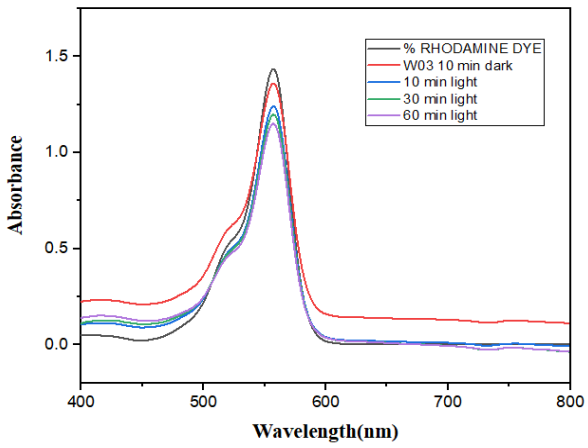


**(a)**

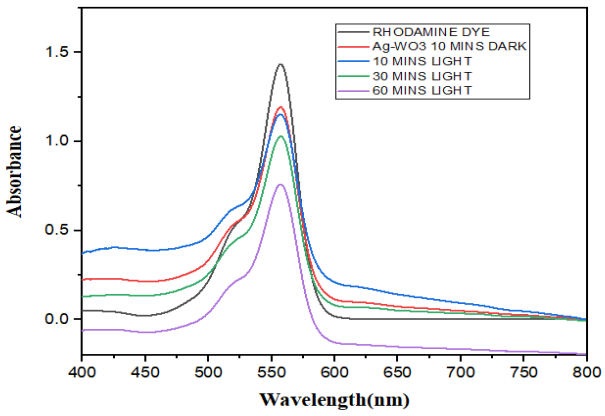


**(b)**

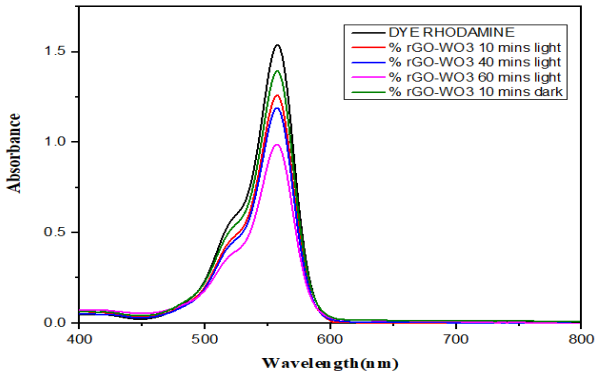


**(c)**

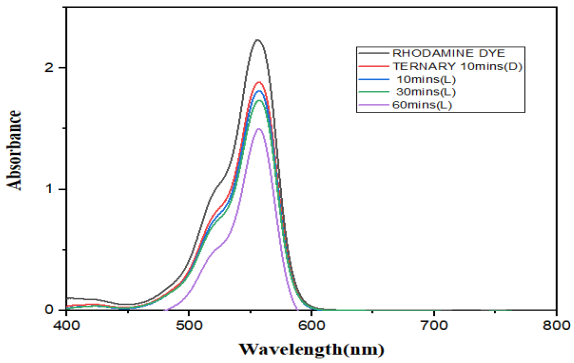


**(d)**

**Fig 3.12** Absorption spectra of Congo red dye in the presence of light (a) $WO_3$ (b) Ag-$WO_3$ (c) rGO-$WO_3$ (d) Ag-$WO_3$-rGO

Table 3.5.shows the degradation efficiency of the samples $WO_3$, Ag-$WO_3$, rGO-$WO_3$ and ternary Ag-$WO_3$-rGO respectively in RhB.

**Table 3.5.** Degradation efficiency of $WO_3$, Ag-$WO_3$, rGO-$WO_3$ and Ag-$WO_3$-rGO in RhB

| **Samples** | **Degradation efficiency (60 min)** |
|---|---|
| TERNARY **(10 mg)** | 40.25% |
| Ag-$WO_3$ **(25 mg)** | 46.85% |
| rGO-$WO_3$ **(25 mg)** | 36.12% |
| WO3 **(25mg)** | 23.25% |

Figure 3.13 shows the degradation RhB curve of $WO_3$, Ag-$WO_3$, rGO-$WO_3$ and ternary Ag-$WO_3$-rGO under visible irradiation. . In the figure time was plotted along the X axis, $\frac{C_t}{C_0}$ was plotted along the Y axis. $C_0$ (mg/L) is the initial concentration before irradiation by light and $C_t$ (mg/L) is the instantaneous concentration in the sample at time t.

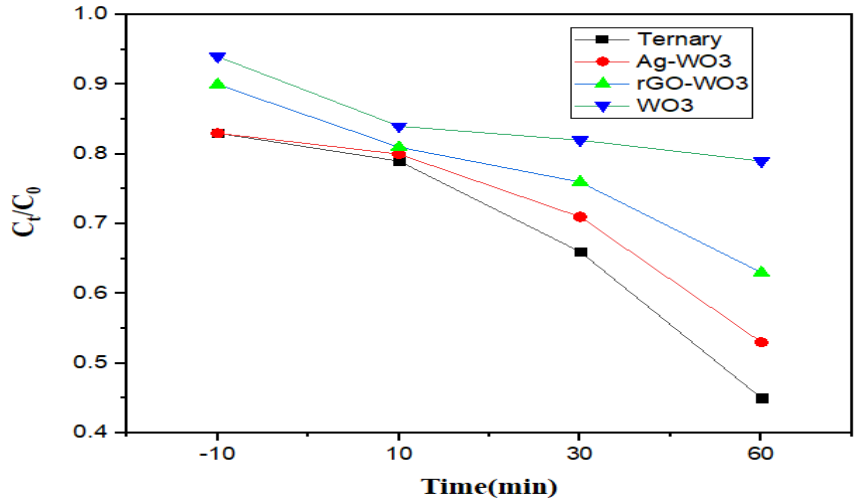


**Fig 3.13** Degradation curve of RhB with $WO_3$ and its nanocomposites

### 3.6.4 Mechanism of adsorption and photocatalytic activity of $WO_3$ and its nanocomposites on Rhodamine B

When $WO_3$ is doped with Ag, it is seen that Ag acts as an electron reservoir that effectively contributes for enhancing the photocatalytic performance of Ag-$WO_3$. In the case of rGO-$WO_3$ the addition of rGO into $WO_3$ would increase the specific surface area of photocatalyst. Moreover due to π - π interaction between the RhB and the benzene rings of rGO, there will be more interaction between the dye and rGO which could enhance the adsorption of RhB in rGO-$WO_3$ [3]. The hydrogen-bonding interactions between H (δ+) of rGO and $OH^-$ (δ-) of RhB can also contribute to the enhanced adsorption [4].

The photocatalytic degradation mechanism of RhB dye solution by the $WO_3$ photocatalyst under visible light irradiation can be discussed by Equations (3.5) to (3.10)

$$WO_3 + h\nu = WO_3\,(h^+(vb) + e^-(cb)) \quad \text{(3.5)}$$

$$WO_3(e^-(cb)) + O_2 = WO_3 + .O_2^- \quad \text{(3.6)}$$

$$.O_2^- + H^+ = .HO_2 \quad \text{(3.7)}$$

$$WO_3\ (e^-\ (\mathrm{vb})) + .\mathrm{HO_2} + \mathrm{H^+} = \mathrm{H_2O_2} \quad \text{(3.8)}$$

$$H_2O_2 + WO_3\ (\mathrm{e^-\ (cb)}) = .\mathrm{OH} + \mathrm{OH^-} \quad \text{(3.9)}$$

$$O_2^-/.\mathrm{OH} + \mathrm{dye} = \mathrm{products} \quad \text{(3.10)}$$

When $WO_3$ is irradiated with visible radiation, an electron in the valence band excites to the conduction band and a hole is created in the valence band. The electrons at the photocatalyst surface were prohibited by the molecular oxygen to produce the superoxide radical anion $.O_2$ as shown in equation (3.6). The superoxide radical anion $.O_2$, further combines with H to generate $.HO_2$. Finally, the photocatalytic degradation of the dye takes place through equation (3.10).The active oxygen species (.OH, $.HO_2$ or $.O_2$ radicals) and the dyes were degraded gradually. The dye adsorbs the proton and protonates and this protonation continues and the degraded products are obtained after the certain period of time [7,8].

When $WO_3$ is doped with Ag, it has more defects on its grain boundary and the band gap of Ag-$WO_3$ is lowered and can be excited more by the visible light, thereby exciting more valence electrons up to the conduction band and leaving holes in the valence band [9,10]. The holes remaining in the valence band can interact with the electrons from $OH^-$ or water molecules to form hydroxyl radicals (.OH). The electrons in the conduction band (or doped Ag) can combine with the dissolved oxygen to form $O_2^-$. Then, both the .OH and $O_2^-$ can contribute to the degradation RhB molecules as given in equation (3.10).

In the case of rGO-$WO_3$ and Ag-$WO_3$-rGO, the addition of rGO restricts the recombination of the photogenerated electron-hole pairs, thereby improving the photocatalytic activity of the ternary Ag-$WO_3$-rGO nanocomposite [4].

# REFERENCES

(1) Faiz, MS Amir, CA Che Azurahanim, Syahidah Azis Raba'ah, and Mohd Zawawi Ruzniza. "Low cost and green approach in the reduction of graphene oxide (GO) using palm oil leaves extract for potential in industrial applications." *Results in Physics* 16 (2020): 102954.

(2) Mohammed Harshulkhan, S., K. Janaki, G. Velraj, R. Sakthi Ganapthy, and M. Nagarajan. "Effect of Ag doping on structural, optical and photocatalytic activity of tungsten oxide ($WO_3$) nanoparticles." *Journal of Materials Science: Materials in Electronics* 27, no. 5 (2016): 4744-4751.

(3) Fu, Li, Tian Xia, Yuhong Zheng, Jun Yang, Aiwu Wang, and Zhong Wang. "Preparation of $WO_3$-reduced graphene oxide nanocomposites with enhanced photocatalytic property." *Ceramics International* 41, no. 4 (2015): 5903-5908.

(4) Tran, Vy Anh, Thang Phan Nguyen, Il Tae Kim, Sang-Wha Lee, and Cong Tu Nguyen. "Excellent photocatalytic activity of ternary Ag@ $WO_3$@ rGO nanocomposites under solar simulation irradiation" *Journal of Science: Advanced Materials and Devices* 6, no. 1 (2021): 108-117.

(5) Nguyen, Cong Tu, Tuan Phong Pham, Thi Lan Anh Luu, Xuan Sang Nguyen, Thanh Tung Nguyen, Huu Lam Nguyen, and Duc Chien Nguyen. "Constraint effect caused by graphene on in situ grown Gr@ $WO_3$-nanobrick hybrid material" *Ceramics International* 46, no. 7 (2020): 8711-8718.

(6) Alaei, Mahshad, Ali Reza Mahjoub, and Alimorad Rashidi. "Effect of $WO_3$ nanoparticles on congo red and rhodamine B photo degradation." (2012): 23-29.

(7) Jeyapaul, T., K. Prakash, S. Harikengaram, A. Chellamani, and V. Selvam. "Synthesis of $WO_3$ nanorods and their photocatalytic degradation of organic contaminants." *Rasayan J. Chem* 11, no. 4 (2018): 1405-1414.

(8) Ke, Dingning, Huajun Liu, Tianyou Peng, Xun Liu, and Ke Dai. "Preparation and photocatalytic activity of $WO_3$/$TiO_2$ nanocomposite particles." *Materials Letters* 62, no. 3 (2008): 447-450.

(9) Matalkeh, Maha, Gheyath K. Nasrallah, Farah M. Shurrab, Enas S. Al-Absi, Widad Mohammed, Ahmed Elzatahry, and Khaled M. Saoud. "Visible light photocatalytic activity of

$Ag/WO_3$ nanoparticles and its antibacterial activity under ambient light and in the dark." *Results in Engineering* 13 (2022): 100313.

(10) Maha, Matalkeh, Gheyath K. Nasrallah, Farah M. Shurrab, Enas S. Al-Absi, Widad Mohammed, Ahmed Elzatahry, and Khaled M. Saoud. "Visible Light Photocatalytic Activity of $Ag/WO_3$ Nanoparticles and its Antibacterial Activity Under Ambient Light and in The Dark." (2022).

# CHAPTER – 4

# CONCLUSION AND FUTURE SCOPE OF STUDY

In this work, $WO_3$, Ag-$WO_3$ and rGO-$WO_3$ were synthesized by hydrothermal method and ternary Ag-$WO_3$-rGO was synthesized by two-step hydrothermal method. XRD patterns shows the formation of $WO_3$ with monoclinic structure. The particle size of the samples were measured using Scherrer formula and the particle size lies in the nm scale. SEM images shows uniform nanoparticles and the SEM images of $WO_3$ and Ag-$WO_3$ shows spherical morphology. In the case of rGO-$WO_3$ it was observed that $WO_3$ nano particles were randomly distributed on rGO sheets. The SEM image of GO shows that the graphene sheets are exfoliated in graphene oxide. EDX shows the elemental information of the prepared samples and the presence of the doped materials Ag/rGO on $WO_3$.

Raman spectra gives an idea about the vibrational energy level of the samples. The observed Raman peaks confirms the monoclinic structure of $WO_3$. Some peaks of $WO_3$ were seen shifted to the lower wavenumber when $WO_3$ was doped with Ag. The Raman spectra of GO shows the presence of D band and G band and these bands were observed in the case of rGO-$WO_3$ also. It was observed that when rGO was introduced to $WO_3$ and Ag-$WO_3$, there was a red shift of the G band.

The photocatalytic activity of $WO_3$, Ag-$WO_3$, rGO-$WO_3$ and ternary Ag-$WO_3$-rGO in aqueous Congo red dye solution and Rhodamine B solution were studied. The results show that Ag-$WO_3$ and ternary nanocomposite show excellent degradation of Congo red dye and Rhodamine B under visible light irradiation. The presence of Ag and rGO nanosheets in the $WO_3$-based nanocomposites did not affect the morphology and crystal structure but have rendered the electron transfer and the optical absorption properties. The optical bandgap of the samples were reduced when $WO_3$ was doped with Ag/rGO which enhanced the photocatalytic activities. The degradation efficiency was observed more in the case of Congo red dye within a given time interval compared with Rhodamine dye.

$WO_3$ have few drawbacks due to smaller specific surface area and high recombination rate of photo generated electron hole pairs. This has limited the photocatalytic activity of $WO_3$. These drawbacks can be improved by developing various $WO_3$ – based materials to improve their performance. $WO_3$ can be used for various other uses like storage cells, gas sensors etc. Some

methods can be devised to improve its electrical properties and optical properties so that it can be used for making more efficient photodetectors, light-emitting diodes (LED) etc.